



Igneous layering and magma dynamics in alkaline intrusions: textural evidence for gravitational settling and compaction within cumulates


Emily Jones^{1*}, William McCarthy¹, Craig Magee², Tobias Mattsson³, Sandra Piazzolo², William Hutchison¹ and Madeleine C.S. Humphreys⁴

¹ School of Earth and Environmental Sciences, University of St Andrews, St Andrews KY16 9TS, UK

² School of Earth and Environment, University of Leeds, Leeds LS2 9JT, UK

³ Department of Earth Sciences, Uppsala University, Uppsala 752 36, Sweden

⁴ Department of Earth Sciences, Durham University, Durham DH1 3LE, UK

 EJ, 0009-0002-4086-5845; WM, 0000-0002-7214-1449; CM, 0000-0001-9836-2365; TM, 0000-0003-0717-4014; SP, 0000-0001-7723-8170; WH, 0000-0002-5456-3277; MCSH, 0000-0001-9343-1237

* Correspondence: em208@st-andrews.ac.uk

Abstract: The mechanisms responsible for igneous layering and the concentration of critical minerals within alkaline intrusions remain a matter of debate. The Ilímaussaq complex, South Greenland, is a layered alkaline intrusion containing economically important deposits of rare earth elements. Based on geochemical and petrological data, the two leading hypotheses for the formation of igneous layering at Ilímaussaq are: (1) repeated magma recharge and the *in situ* nucleation of minerals; or (2) the gravitational settling of crystal mats within a closed magmatic system. We provide novel field, rock magnetic and crystallographic preferred orientation data from two representative outcrops of igneous layering at Ilímaussaq to test these hypotheses. Our rock magnetic data show that both arfvedsonite and magnetite contribute to the anisotropy of magnetic susceptibility fabrics, with magnetite defining a subvertical foliation across the igneous layering. Our data show that the anisotropy of magnetic susceptibility fabric is inverse to the silicate fabric (i.e. the magnetic foliation is normal to the silicate foliation) and records consistent sub-horizontal mineral foliations and lineations vertically through the layers. Crucially, the silicate fabric is often oblique in both strike and dip to the modal igneous layering. Our measured fabrics best support a closed system crystal mat model and subsequent phases of differential and intrusion-wide compaction.

Supplementary material: Two supplementary figures are available at <https://doi.org/10.6084/m9.figshare.c.7618284>

Received 6 September 2024; revised 30 January 2025; accepted 4 April 2025

Layered igneous intrusions preserve detailed records of the physical and chemical processes within magma reservoirs (e.g. Irvine 1980; Tait and Jaupart 1992; Naslund and McBirney 1996; Namur *et al.* 2015; Nielsen *et al.* 2015; Latypov *et al.* 2017; O'Driscoll and Van Tongeren 2017; Smith and Maier 2021). To date, the vast majority of studies have focused on layered intrusions that are mafic to ultramafic in composition (e.g. Boudreau and McBirney 1997; O'Driscoll *et al.* 2008; Holness *et al.* 2012, 2017; Nielsen *et al.* 2015; Latypov *et al.* 2017; Vukmanovic *et al.* 2019). Yet even for well-studied layered intrusions, such as the Stillwater Complex (USA), the Bushveld Complex (South Africa), the Skaergaard intrusion (Greenland) and Rum (Scotland), their complex petrography means there is often a lack of consensus on how the igneous layering formed (e.g. Boudreau 1988; Eales and Cawthorn 1996; O'Driscoll *et al.* 2008; Latypov *et al.* 2017; Smith and Maier 2021). By contrast, alkaline layered intrusions, which can host important economic rare earth element (REE) deposits within their layers, have scarcely been investigated (e.g. Marks and Markl 2015; Hunt *et al.* 2017; Borst *et al.* 2018; O'Driscoll *et al.* 2024). Exploring and targeting such REE deposits requires an in-depth understanding of the geological environments and processes that concentrate REEs within alkaline layered intrusions.

The origins of layering in igneous intrusions have primarily been studied using geochemical and mineralogical approaches (e.g. Duchesne and Charlier 2005; Pang *et al.* 2009; Borst *et al.* 2018). However, these data are often ambiguous when interpreting the dominant layering mechanisms (e.g. Boorman *et al.* 2004). An

alternative approach is to quantify the igneous textures, particularly the orientation and alignment of the crystal phases (i.e. petrofabrics) (e.g. Branagan 2005; O'Driscoll *et al.* 2008, 2015). These data enable us to quantitatively decipher the crystallization history, magma reservoir processes and tectonic activity within igneous systems (e.g. Branagan 2005; O'Driscoll *et al.* 2008; Petronis *et al.* 2012; Biedermann *et al.* 2016; Holness *et al.* 2017; O'Driscoll and Van Tongeren 2017; Holness 2018; Mattsson *et al.* 2021). However, identifying fabrics within igneous rocks is often difficult in the field due to the exposure, grain size and crystalline texture.

Anisotropy of magnetic susceptibility (AMS) provides a means of measuring magnetic fabrics, even when mesoscopic- to macroscopic-scale fabrics are not visible, in a fast, non-destructive and three-dimensional manner (e.g. Borradaile 1988; Knight and Walker 1988; Tarling and Hrouda 1993; Dunlop and Özdemir 1997; Borradaile and Jackson 2004; O'Driscoll *et al.* 2015; Bilardello 2016; Magee *et al.* 2016; Koopmans *et al.* 2022). AMS functions as a tool for recording petrofabrics because most minerals are magnetically anisotropic – that is, they are easier to magnetize in certain orientations depending on their crystallography and grain shape (e.g. Borradaile and Jackson 2004; Martín-Hernández *et al.* 2004; O'Driscoll *et al.* 2008).

Here, we examine the Ilímaussaq complex, a layered alkaline intrusion located in South Greenland (Andersen *et al.* 1981; Bailey *et al.* 2001; Sørensen 2001; Upton 2013; Marks and Markl 2015). Ilímaussaq was emplaced at c. 1.2 Ga as part of the Gardar alkaline province and is of particular interest because its layered suite hosts

world-class ore deposits containing REEs, Zr, Nb, Hf, Ta, U, Li, Be, Zn and Th (e.g. Larsen and Sørensen 1987; Bailey *et al.* 2001; Sørensen 2001; Sørensen *et al.* 2011; Schönwandt *et al.* 2016; Borst *et al.* 2018). Two competing models have been proposed to explain the layering at Ilímaussaq: one model involves pulsed magmatic injection and *in situ* crystallization in an open system environment (Hunt *et al.* 2017), whereas the other invokes crystal mat formation and gravitational settling in a closed system (Bons *et al.* 2015; Lindhuber *et al.* 2015; Marks and Markl 2015; Borst *et al.* 2018). Recent work on a small suite of samples from Ilímaussaq demonstrated that AMS accurately records the fabrics in the highly evolved nepheline syenites (O'Driscoll *et al.* 2024). We provide the first comprehensive field and rock magnetic study of several layer packages at Ilímaussaq, with exceptionally high spatial resolution, to test the open and closed system layering hypotheses. We show that the rock fabric best supports the latter hypothesis where layers form through crystal mats, in combination with compaction of the crystal mush, which modifies the layering.

Geological setting

The Ilímaussaq complex

The Ilímaussaq complex is a layered peralkaline (molar $(\text{Na} + \text{K})/\text{Al} > 1$) intrusion within the Gardar igneous province of South Greenland. The complex formed during two continental rifting events associated with the 1300–1100 Ma break-up of the Columbia–Nuna supercontinent (Fig. 1) (e.g. Upton *et al.* 2003; Marks *et al.* 2011; Upton 2013; Marks and Markl 2015). The Ilímaussaq complex is oval shaped in map view and c. 17 km × 8 km in size. It was emplaced at c. 3–4 km depth between the granitic Julianehåb batholith (c. 1800 Ma) and the overlying terrestrial sandstones and lavas of the Eriksfjord Formation (c. 1300–1270 Ma) (Garde *et al.* 2002; Krumrei *et al.* 2006; Upton 2013). The magma was intruded between 1165 and 1155 Ma and the melt–mush system was likely active for c. 1 Ma (Krumrei *et al.* 2006; Borst *et al.* 2019). No evidence of post-emplacement deformation has been recorded at Ilímaussaq, making it an ideal

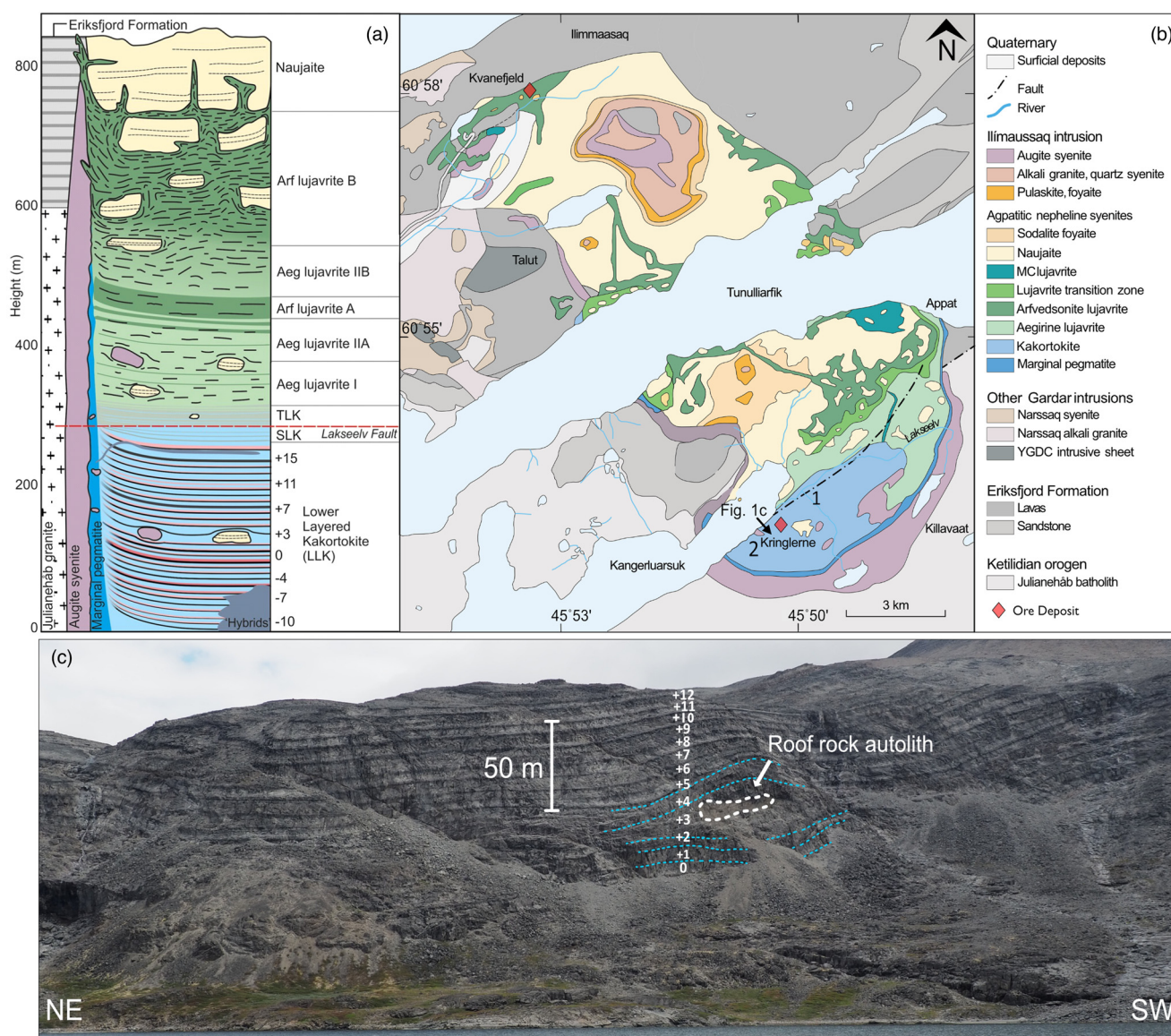


Fig. 1. (a) Schematic cross-section through the Ilímaussaq complex, South Greenland. (b) Geological map of the Ilímaussaq complex with the locations of the rare earth element deposits marked by red diamonds. Labels 1 (Laksetværelv) and 2 (Kringlerne) mark the locations of the two study areas. (c) Panoramic photograph of the lower layered kakortokites with units 0 through +12 labelled. The blue dotted lines highlight the layers deflecting around the autolith. TLK, Transitional layered kakortokite; SLK, slightly layered kakortokite; YGDC, younger giant dyke complex. Source: part (a) modified after Borst *et al.* (2018) and Andersen *et al.* (1981); part (b) modified after Upton (2013).

natural laboratory to investigate primary alkaline magmatic processes (Upton *et al.* 2003; Upton 2013; Marks and Markl 2015).

The Ilímaussaq complex is famous for its mineral layering and chemically evolved mineralogy. The complex also hosts two world-class ore deposits: Kvanefeld contains *c.* 1 billion tonnes of total rare earth oxide, U and Zn mineralization, whereas Kringlerne contains *c.* 4.5 billion tonnes of total rare earth oxide, Zr and Nb mineralization (Fig. 1) (Sørensen 2001; Borst *et al.* 2016; Schönwandt *et al.* 2016). The Ilímaussaq complex formed through the emplacement of at least four batches of magma: (1) an initial batch of augite syenite, which occurs around the perimeter of the complex; (2) a peralkaline granite and quartz syenite, which occur in the roof of the complex; (3) peralkaline nepheline syenites, which also occur within the roof horizon; and (4) a separate batch of peralkaline nepheline syenites that comprises the floor and ‘sandwich’ horizons (Fig. 1) (e.g. Sørensen *et al.* 2006; Pfaff *et al.* 2008; Ratschbacher *et al.* 2015; Borst *et al.* 2018). The nepheline syenites are the most well-studied part of the complex because they display significant layering and host the REE deposits (e.g. Bailey *et al.* 2001; Sørensen 2001; Hunt *et al.* 2017; Borst *et al.* 2018). Within the nepheline syenites, the roof and ‘sandwich’ horizons are locally referred to as naujaite and lujavrite, respectively (Fig. 1). The floor horizon, locally referred to as kakortokite (Fig. 1), is the focus of our study because it displays the most well-defined igneous layering.

The kakortokites are divided into three sequences (Fig. 1a): the >220 m thick lower layered kakortokites, slightly layered kakortokites and transitional layered kakortokites (e.g. Bohse *et al.* 1971; Marks and Markl 2015; Borst *et al.* 2018). The focus of our study is the lower layered kakortokites, which display well-defined layers of two types: (1) an *c.* 8 m thick three-layer unit characterized by variations in the modal abundances of arfvedsonite (inosilicate, monoclinic), eudialyte

(cyclosilicate, trigonal), alkali feldspar (tectosilicate, monoclinic/triclinic) and nepheline (tectosilicate, hexagonal); and (2) the repetition of this three-layer unit a minimum of 29 times throughout the sequence (e.g. Bohse *et al.* 1971; Sørensen 2001; Marks and Markl 2015; Hunt *et al.* 2017). Each three-layer unit typically contains a black arfvedsonite-rich layer at its base, a red layer in the centre rich in eudialyte group minerals and a white alkali feldspar- and nepheline-rich layer at the top; some units do not contain the red layer rich in eudialyte group minerals (Bohse *et al.* 1971). Each three-layer unit has been labelled –11 to +17 with respect to unit 0, which is commonly accepted as the most well-developed three-layer unit in the sequence (e.g. Bohse *et al.* 1971; Sørensen 2001; Hunt *et al.* 2017; Borst *et al.* 2018). The layered unit +3 contains roof rock autoliths that the layers above and below deflect around (Fig. 1) (e.g. Bohse *et al.* 1971; Andersen *et al.* 1981).

Current models for the formation of kakortokite layering

Models for layering in the Ilímaussaq kakortokites can be divided into two main groups: those supporting an open magmatic system with magma replenishment events and those involving layer formation within a closed magmatic system (e.g. Larsen and Sørensen 1987; Pfaff *et al.* 2008; Lindhuber *et al.* 2015; Marks and Markl 2015; Hunt *et al.* 2017; Borst *et al.* 2018). In the most recently proposed open system model, Hunt *et al.* (2017) used eudialyte group mineral geochemistry and log-linear crystal size distribution data from arfvedsonite and eudialyte in unit 0 to suggest *in situ* nucleation and growth of the black and red layers (Fig. 2a). In this open system model, an injection of a relatively primitive magma pools on the reservoir floor, where high concentrations of halogens inhibit the nucleation of all mineral phases except for arfvedsonite, which crystallizes *in situ* to form the black layer

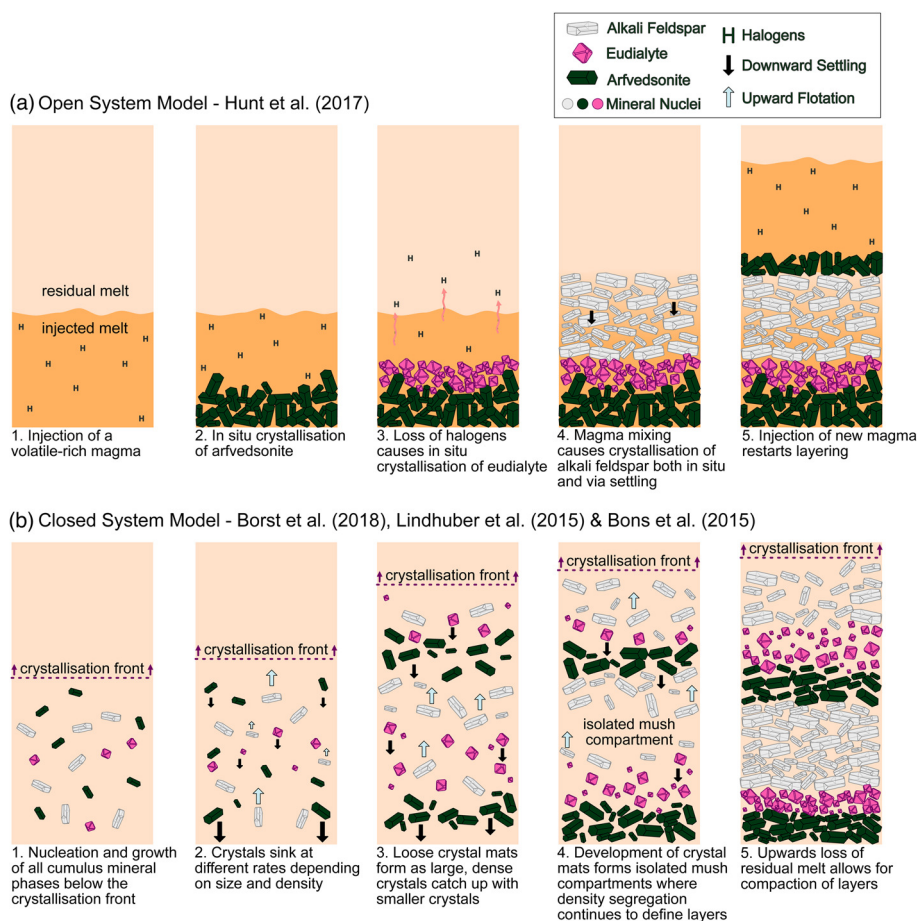


Fig. 2. Schematic diagrams of (a) the open system model and (b) the closed system model. Source: part (a) based on the description by Hunt *et al.* (2017) and part (b) based on descriptions by Borst *et al.* (2018), Bons *et al.* (2015) and Lindhuber *et al.* (2015).

(Fig. 2a) (Hunt *et al.* 2017). As halogens transfer from the injected magma into the overlying residual magma, eudialyte becomes stable and crystallizes *in situ* to form the red layer (Fig. 2a) (Hunt *et al.* 2017). Cooling of the injected magma leads to its thermal equilibration with the resident magma. Alkali feldspar and nepheline begin to nucleate, both *in situ* and suspended in the newly mixed magma, forming the white layer (Fig. 2a) (Hunt *et al.* 2017). The repetition of these three-layer units is suggested to represent new magma replenishment events with minimal compositional variations (Hunt *et al.* 2017).

Alternatively, a closed system model has been suggested in which crystal mat formation is the main layering mechanism within the kakortokites (Fig. 2b) (Bons *et al.* 2015; Lindhuber *et al.* 2015; Marks and Markl 2015; Borst *et al.* 2018). In this closed system model, cumulate minerals nucleate and grow below a rising crystallization front. Heavier minerals (such as arfvedsonite and eudialyte) sink, while lighter minerals (such as alkali feldspar) float (Fig. 2b) (Bons *et al.* 2015; Lindhuber *et al.* 2015; Borst *et al.* 2018). As crystallization continues, larger and heavier crystals catch up with the smaller crystals sinking below them (i.e. hindered settling) and begin to form loosely aggregated mats (Fig. 2b) (Bons *et al.* 2015; Lindhuber *et al.* 2015). The crystal mats form progressively from the bottom of the magma reservoir upwards (Borst *et al.* 2018). With time, the crystal mats grow and the acicular crystal habit of arfvedsonite forms dense mats and the more tabular habit of alkali feldspar forms looser, more porous mats (Lindhuber *et al.* 2015).

Continued crystallization, including the crystallization of intercumulus material within the mats, forms quasi-closed mush systems (Bons *et al.* 2015; Lindhuber *et al.* 2015; Marks and Markl 2015; Borst *et al.* 2018). Within these quasi-closed systems, internal melt fractionation and gravitational settling further segregate the main cumulus minerals into three-layer units (Fig. 2b) (Bons *et al.* 2015; Lindhuber *et al.* 2015; Borst *et al.* 2018). Although this closed system model is well supported by geochemical data, the *in situ* crystallization recorded by the crystal size distribution data, integral to the open system model, is at odds with the suggested gravitational settling.

Predicted rock fabrics for existing layer formation hypotheses

The competing hypotheses for the layering of the kakortokites hinge on mechanical processes that are expected to be reflected in the rock fabric data (Figs 2, 3) (Meurer and Boudreau 1998). Potential fabrics that may be observed are: (1) mineral foliations defined by the alignment of minerals along a plane; (2) mineral lineations defined by the alignment of mineral long axes; and (3) modal layer contacts defined by variations in mineral abundances (e.g. Higgins 1991; Meurer and Boudreau 1998). Here, we predict the rock fabrics likely

to result from the proposed layering hypotheses and compare these with the field and rock magnetic fabric data collected in this study.

The open system model suggests that the black and red layers form through *in situ* crystallization and the white layers form through a combination of gravitational settling and *in situ* crystallization (Hunt *et al.* 2017). The closed system model suggests that gravitational settling is the main layering mechanism for the black, red and white layers. *In situ* nucleation and growth will typically produce no (i.e. an isotropic) fabric (Meurer and Boudreau 1998), whereas the gravitational settling of crystals will produce a mineral foliation (e.g. Hess 1960; Jackson 1961; Meurer and Boudreau 1998). The open system model would therefore likely produce no fabric in the black and red layers and potentially foliations within the white layers (Fig. 3a). By contrast, the closed system model would likely produce near-horizontal foliations across all layers (Fig. 3b) (Meurer and Boudreau 1998). Crucially, magmatic fabrics may be modified by processes such as: (1) magmatic flow over the crystal pile; (2) post-crystallization compaction of the crystal pile; or (3) pre-consolidation shearing along inclined surfaces (e.g. Young and Donaldson 1985; Higgins 1991; Meurer and Boudreau 1998). We therefore also explored the potential impacts of these processes.

Methodology

Sampling and logging

To record the structural, textural and modal mineral variations in the kakortokites, we collected oriented core samples and stratigraphic logs during a six-week expedition to Ilimaussaq in 2022. High spatial resolution sampling and logging were focused on two localities where unit 0, which contains the clearest igneous layering in the field (Bohse *et al.* 1971), is well exposed. At locality 1 (Laksetværelv), sampling and logging were conducted across layers -1W, 0B, 0R, 0W and +1B (where W represents the white, B the black and R the red layers) (Fig. 4). At locality 2 (Kringlerne Cliff), unit 0 was sampled and logged at a lower resolution relative to locality 1 due to the nature of the outcrop, but more units were studied, including layers -1W, 0B, 0R, 0W, +1B, +1R, +1W, +2B, +2R and +2W (Fig. 4). Where possible, core samples were collected perpendicular to the observed modal layering and stratigraphic logging was conducted along the sampling transect. Sampling was conducted with a hand-held drill with a 25 mm diameter non-magnetic diamond-tipped drill bit. Core orientations were measured using a Pomeroy orienting fixture. Sample locations were recorded using GPS and on 1:100 scale window maps. Standard 25 mm × 21 mm cylindrical sub-specimens were cut from the core samples at the University of St Andrews using a non-magnetic diamond-edged circular saw.

Rock magnetic analyses

An essential part of all rock magnetic studies is determining the relationship between the magnetic fabric and the crystal fabric. Typically, the magnetic long and short axes are parallel to the crystal long and short axes, respectively, meaning we can use AMS to measure petrofabric orientations (e.g. Tarling and Hrouda 1993). However, although AMS is a useful tool, it provides a mean magnetic measurement of a sample and therefore combines the magnetic contributions of all the diamagnetic, paramagnetic and ferromagnetic minerals in a rock (e.g. Tarling and Hrouda 1993; O'Driscoll *et al.* 2008; Bilardello 2016). Therefore it may lead to complications if: (1) multiple fabrics are present within a sample (i.e. the AMS will only record one, possibly hybrid, fabric); (2) the dominant magnetic minerals have an inverse AMS (e.g. single-domain magnetite), whereby the magnetic long and short axes are

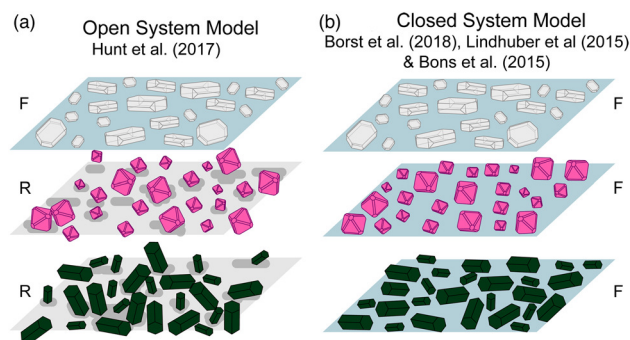


Fig. 3. Predicted rock fabrics in layers formed from different layering models. Random crystal orientations (R) shown in grey; crystal foliation (F) shown in blue. Source: part (a) as described by Hunt *et al.* (2017); part (b) as described by Borst *et al.* (2018), Lindhuber *et al.* (2015) and Bons *et al.* (2015).

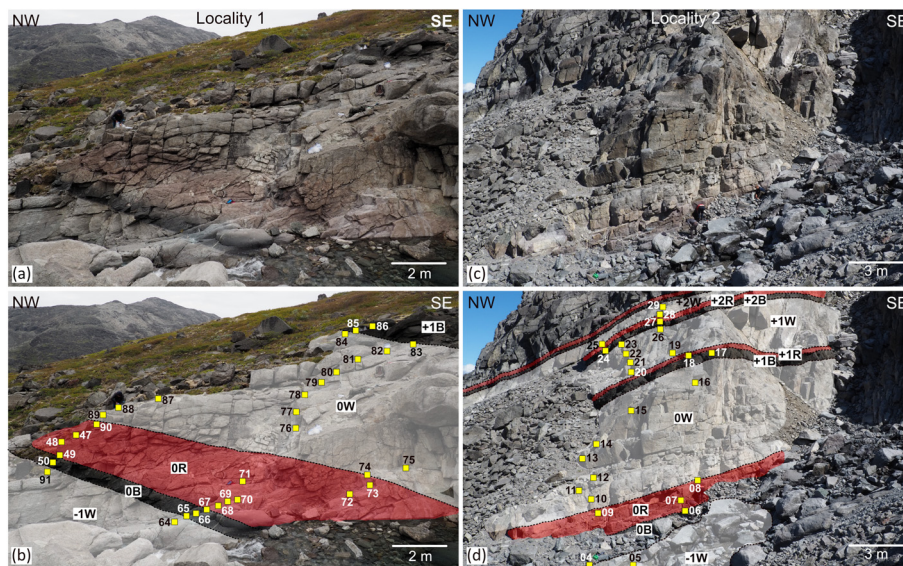


Fig. 4. (a) Photograph of locality 1. (b) Annotated photograph of locality 1 with layer interpretation, layer labels and sample locations (yellow squares). (c) Photograph of locality 2. (d) Annotated photograph of locality 2. Both localities are shown on the geological map in Figure 1.

parallel to the crystal short and long axes, respectively (Fig. 5a) (Ferré 2002; Černý *et al.* 2020); or (3) the mineral properties, such as the chemistry, abundance, mineral alignment and grain size, cause the AMS fabric to be oblique to the petrofabric (Biedermann *et al.* 2015a, b, 2018; Bilardello 2016; Biedermann 2018). For example, cation substitutions in amphiboles result in contrasting unit cell structures with differing responses to external magnetic fields and AMS analysis (Biedermann *et al.* 2015a; Biedermann 2018). It is therefore essential to characterize the mineral phases that dominate an AMS response and use other forms of textural analysis, such as crystallographic preferred orientation (CPO), to interrogate the AMS data (e.g. O'Driscoll *et al.* 2008, 2015). Measuring the ferromagnetic mineral fabric in isolation, to determine whether the AMS is magnetically inverse or if there are multiple competing fabrics, is therefore highly beneficial and is achieved here using anisotropy of magnetic remanence (e.g. Jackson 1991; Mattsson *et al.* 2021).

AMS analyses

The AMS tensor, which can be represented by an ellipsoid, has three principal susceptibility axes: $K_1 \geq K_2 \geq K_3$ (Fig. 5a) (Tarling and Hrouda 1993). The following parameters, based on the principal susceptibility axes and their corresponding natural logarithms (n_1 ,

n_2 , n_3) can be used to describe the AMS tensor:

$$\text{Mean susceptibility, } K_{\text{mean}} = (K_1 + K_2 + K_3)/3 \quad (1)$$

(Tarling and Hrouda 1993)

$$\text{Degree of anisotropy, } P_j = [(n_1 - n)^2 + (n_2 - n)^2 + (n_3 - n)^2] \quad (2)$$

(Jelinek 1981)

$$\text{Shape factor, } T = (2n_2 - n_1 - n_3)/(n_1 - n_3) \quad (3)$$

(Jelinek 1981)

K_{mean} provides an insight into the mineralogy of the sample because minerals have different susceptibility values depending on whether they are diamagnetic, paramagnetic or ferromagnetic (Tarling and Hrouda 1993). P_j describes the eccentricity of the AMS ellipsoid (i.e. the strength of the fabric) and T describes the shape (prolate or oblate) of the AMS ellipsoid (Fig. 5b).

Low-field AMS and bulk susceptibility measurements were acquired using an AGICO KLY-5A Kappabridge (400 A m⁻¹ peak field, 1220 Hz peak frequency, room temperature) in the M³Ore lab at the University of St Andrews. A total of 369 sub-specimens were analysed from 32 sample sites at locality 1 and 310 sub-specimens were analysed from 26 sample sites at locality 2. The results are reported as mean AMS tensors averaged across a sample site,

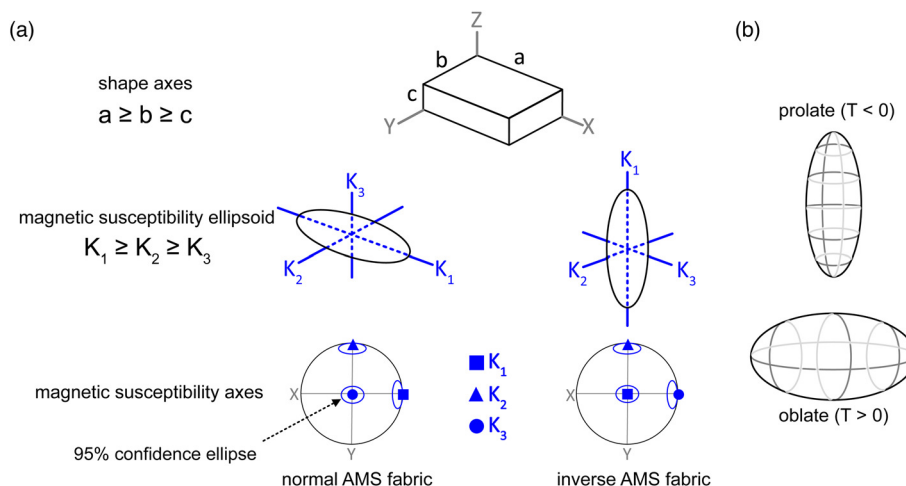


Fig. 5. (a) Relationship between crystallographic and magnetic susceptibility axes for normal and inverse anisotropy of magnetic susceptibility fabrics. (b) Example of prolate and oblate spheroids. AMS, anisotropy of magnetic susceptibility. Source: part (a) adapted from Ferré (2002).

normalized by the mean susceptibility of the sample site (Jelinek 1981). The variability across a sample site is shown with 95% confidence ellipses around the principal axes, calculated by the tensor-averaging method of Jelinek (1981) (Fig. 5a). All processing of the raw data was completed in SAFYR7 software and the data were plotted and the site mean fabric analysed in Anisoft 42.

Magnetic characterization

As AMS is a bulk measurement of all minerals within a sample, temperature susceptibility experiments were conducted to determine the mineral phase that dominates the magnetic susceptibility of the specimens. This is possible because diamagnetic, paramagnetic and ferromagnetic mineral susceptibilities behave differently with temperature (Dunlop and Özdemir 1997). For diamagnetic minerals, the susceptibility does not change with temperature, whereas for paramagnetic minerals, the susceptibility decreases with increasing temperature (Dunlop and Özdemir 1997). The susceptibility of ferromagnetic minerals does not change with temperature until the Curie temperature (T_c) is reached, at which point the susceptibility decreases with temperature (Dunlop and Özdemir 1997).

Temperature susceptibility experiments were conducted on samples from seven representative sites. Samples from a black, red and white layer from both locality 1 and locality 2 were selected, including one duplicate red sample. Sub-specimen off-cuts were crushed using a ceramic pestle and mortar. A c. 0.3 g split of rock pulp was analysed using AGICO CS-L and CS4 attachments to an AGICO KLY-5A Kappabridge. An inducing field of 400 A m^{-1} at 1220 Hz was applied and the bulk magnetic susceptibility was measured every 25 s as each sample was (1) heated from -194°C to room temperature, (2) heated from room temperature to 700°C and cooled back down to room temperature and then (3) heated from -194°C to room temperature again to produce a near-complete heating-cooling system between -194 and 700°C . The raw data were processed using SAFYR 7 software; the holder corrections and Curie point estimates were calculated in Cureval 8.

In addition to the temperature susceptibility experiments, saturation isothermal remanent magnetization (SIRM) and back-field isothermal remanent magnetization (BIRM) measurements were completed on nine representative sub-specimens to assess the coercivity of remanence-carrying particles in the samples (see Dunlop and Özdemir 1997). Duplicate experiments were run on two sub-specimens to ensure consistency of the results. SIRM is achieved by imparting the sub-specimens with a stepwise increasing isothermal remanent magnetization pulse and measuring the remanent magnetization of the sub-specimen between each magnetic pulse. Magnetic pulses are applied to the sub-specimen until it becomes magnetically saturated, at which point the BIRM is measured by applying magnetic pulses in the opposite direction to the SIRM field. Magnetic pulses were applied with an MPM 10 pulse magnetizer and the remanent magnetization was measured with an AGICO JR-6A spinner magnetometer.

Anisotropy of magnetic remanence analysis

To investigate the ferromagnetic fabric only, the anisotropy of anhysteretic remanence (AARM) was completed on 25 representative sub-specimens from locality 1 and 35 representative sub-specimens from locality 2. AARM was completed using the 15-position rotational measurement scheme P-mode outlined by the AGICO REMA6 guidelines (Jelinek 1977). An anhysteretic remanence magnetization (ARM) was applied in 15 sample orientations, with demagnetization steps occurring between each change in orientation. Samples were demagnetized and magnetized with an AGICO LDA5 and PAM1 and the magnetic remanence was measured using a JR-6A

spinner magnetometer. Demagnetization steps were completed with a 200 mT alternating field in an automatic two-axis tumbling specimen holder. ARM was imparted using a $100 \mu\text{T}$ direct current field and a maximum alternating field of 200 mT.

Petrography and CPO

Twenty-eight polished thin sections were created from representative sub-specimen AMS cores to examine the mineral textures and the mineral modal abundances, to determine the cumulus v. intercumulus phases and to assess the relationship between the petrographic and magnetic rock fabric data. Minerals with euhedral grain shapes or impingement textures were considered to be cumulus, whereas minerals with anhedral grain shapes defined by the surrounding impinging minerals were considered to be intercumulus (Wager *et al.* 1960; Higgins 2011). Thin sections were cut parallel to the AMS K_1 and K_3 susceptibility axes and perpendicular to the modal layering to best capture the magnetic foliation and lineation (see [Supplementary Material](#)).

Four polished thin sections were made from sub-specimens to observe the general microstructure and to perform CPO analysis to compare the recorded magnetic fabrics with the measured crystal fabrics. Samples 65 (black layer), 69 (red layer) and 77 (white layer) from locality 1 were selected as representative samples from each layer of unit 0 and sample 24 (black layer) from locality 2 was selected as a representative sample from layer +2B. The CPOs were obtained by electron back-scatter diffraction (EBSD) analyses at the University of Leeds. An FEI Quanta 650 FEG scanning electron microscope with AZtec software and an Oxford Symmetry EBSD detector were used to collect the EBSD maps and energy-dispersive spectra covering roughly 1 cm^2 of the thin sections. The energy-dispersive spectrometry data were used to confirm phases identified by EBSD.

The acquisition settings were 30 kV, 27 mm working distance, 70° specimen tilt and step sizes of 5 and $7 \mu\text{m}$ depending on the grain size. Automatic indexing of arfvedsonite, alkali feldspar, nepheline and eudialyte was completed using AZtec software (Oxford Instruments) and AZtecCrystal was used to complete standard noise reduction and produce pole figures. The pole figures are presented in the ZX plane (see [Supplementary Material](#)), lower hemisphere, 10° contour half-width and a contour range of 0–4 was applied to all the plots. Pole figures were reoriented to the geographical coordinate system for direct comparison with rock magnetic data (see [Supplementary Material](#)). The number of grains identified was in the range of 50–200. All point analyses are shown.

Summary of fabric terminology

- Magnetic long/short axes: these axes refer to the long and short axes of the AMS ellipsoid.
- Crystal long/short axes: these axes refer to the long and short shape axes of a crystal.
- Crystallographic axes ($a <100>$, $b <010>$, $c <001>$): these axes refer to the crystallographic axes of a crystal and do not necessarily correspond in length with the crystal shape axes.
- Silicate mineral fabric: a fabric (foliation and/or lineation) defined by the aligned shape of the silicate minerals within a rock.
- Anisotropy of magnetic susceptibility fabric (AMS K_1 , K_2 , K_3): a magnetic fabric (foliation and/or lineation) defined by the combined contribution of diamagnetic (e.g. feldspar), paramagnetic (e.g. amphibole) and ferromagnetic (e.g. magnetite) minerals within a rock.
- Anisotropy of anhysteretic remanent magnetization fabric (AARM R_1 , R_2 , R_3): a magnetic fabric (foliation and/or lineation) defined solely by the ferromagnetic (e.g. magnetite) minerals within a rock.

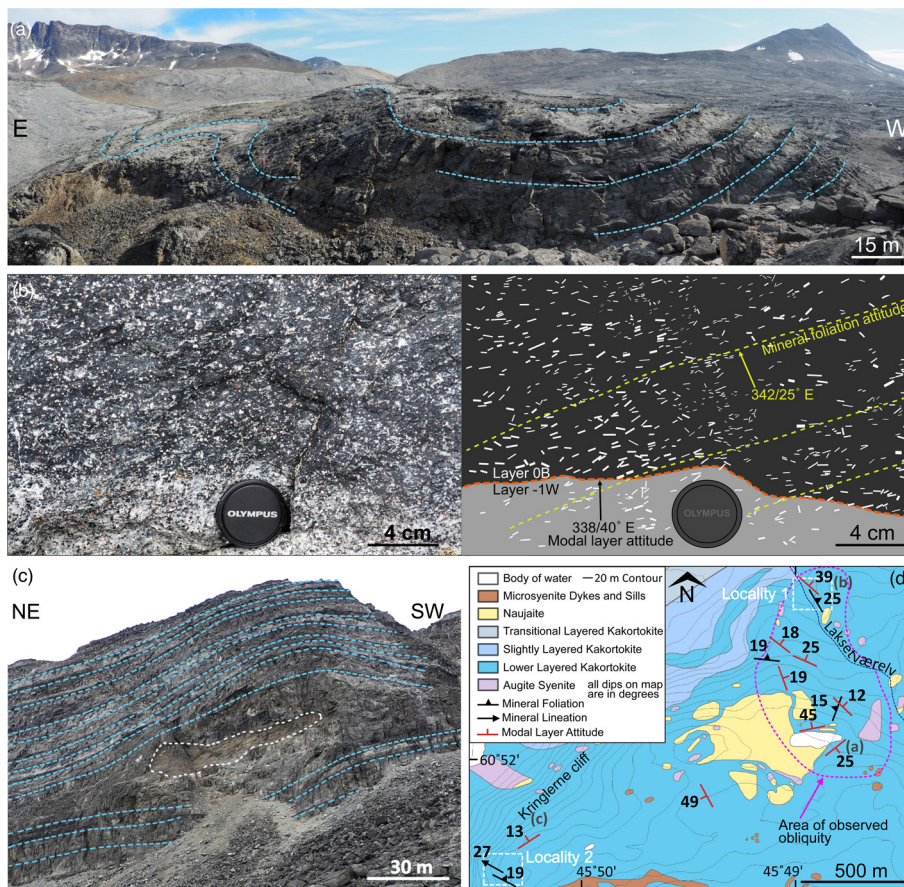


Fig. 6. (a) Panoramic photograph of kakortokite layers showing a bowl-like morphology with the base of the black layers highlighted in blue. (b) Photograph of the layer -1W/layer 0B boundary at locality 1 and annotated photograph with alkali feldspar outlined. (c) Photograph of roof autolith (outlined in white) within kakortokites. Kakortokite layering can be seen deflecting above and below the autolith. The bases of the black layers are highlighted in blue. (d) Structural map of the lower layered kakortokites with locations of photographs in parts (a-c) marked. Source: geological map modified after Andersen *et al.* (1988) and Upton (2013).

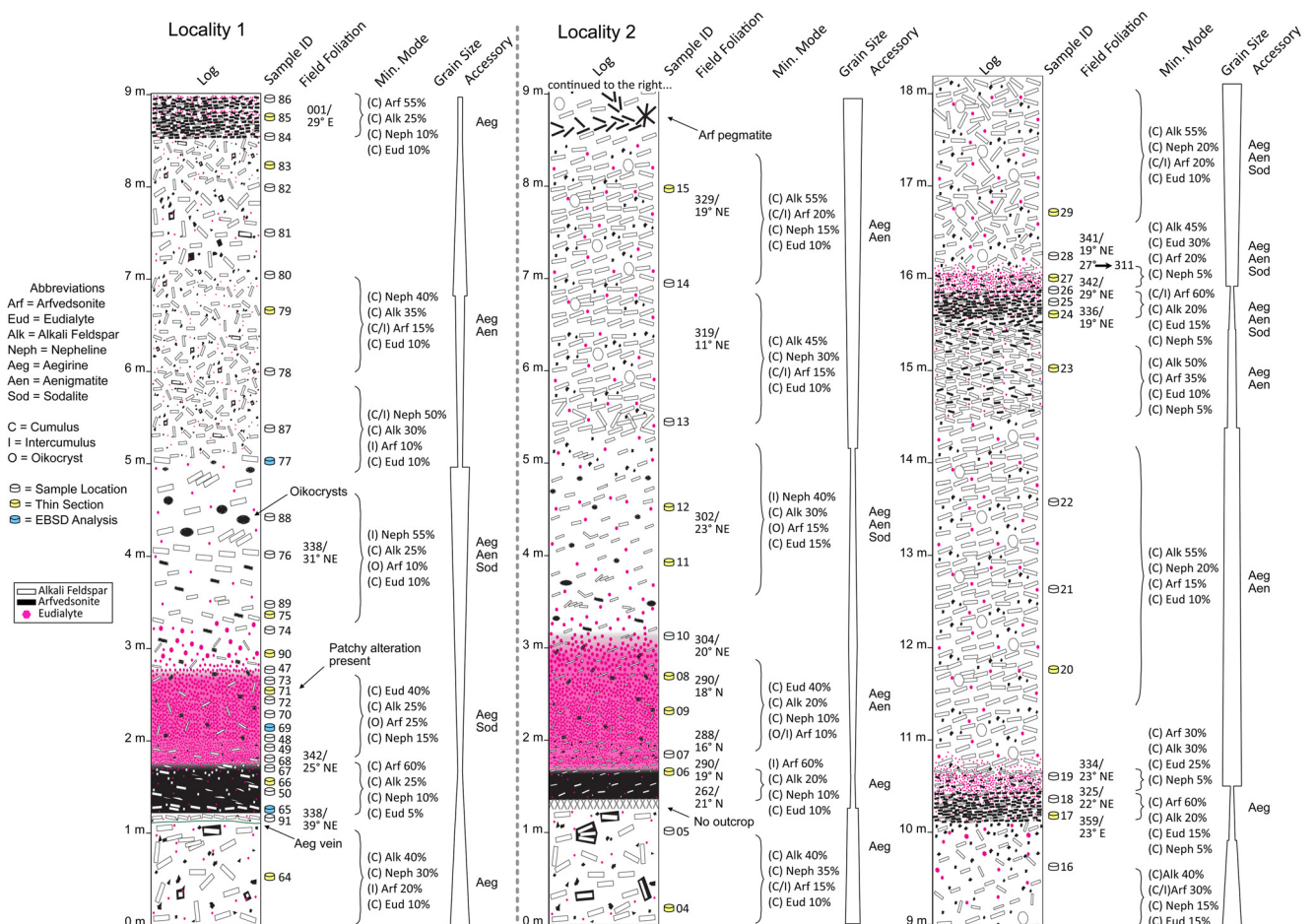


Fig. 7. Geological field logs from localities 1 and 2 in the kakortokites. EBSD, electron back-scatter diffraction.

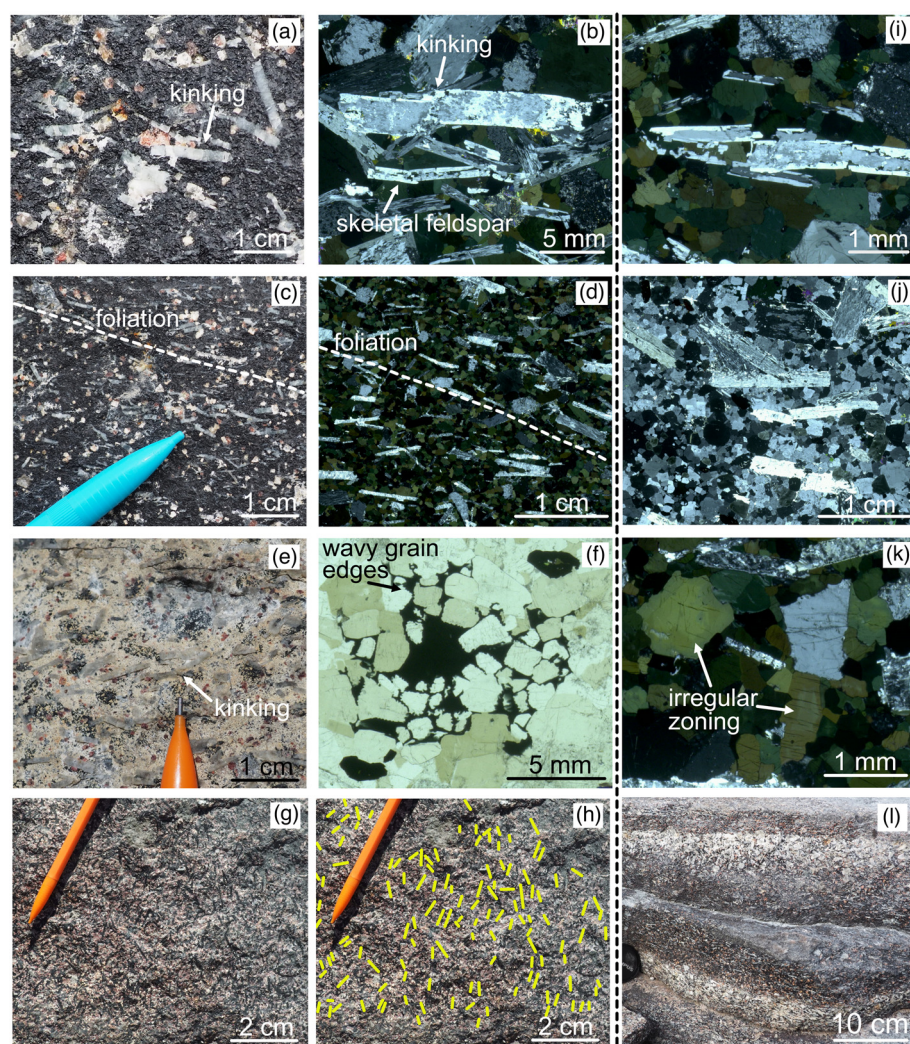


Fig. 8. (a) Photograph of kinked alkali feldspar within layer 0B at locality 1. (b) Cross-polarized light (XPL) thin section image of kinked alkali feldspar from layer -1W at locality 1. (c) Photograph of layer 0B at locality 1 with mineral foliation defined by alkali feldspar. (d) XPL thin section image of foliated alkali feldspar within intercumulus arfvedsonite in layer 0B at locality 1. (e) Photograph of arfvedsonite oikocrysts within layer 0W at locality 2. (f) Plane-polarized light thin section image of arfvedsonite oikocryst with nepheline inclusions. (g) Photograph of aligned arfvedsonite in layer +2R at locality 2. (h) Annotated photograph of aligned arfvedsonite (highlighted in yellow) in layer +2R at locality 2. (i) XPL thin section image of arfvedsonite replacing alkali feldspar in layer 0B at locality 1. (j) XPL thin section image of intercumulus nepheline groundmass and deformed alkali feldspar at the base of layer 0W at locality 1. (k) XPL thin section image of patchy zoning of arfvedsonite in layer 0B at locality 1. (l) Photograph of centimetre-scale layering within kakortokites, with the layering defined by the higher modal abundance of arfvedsonite.

Results

Field observations

We identified that the attitude of the modal layering is spatially variable and a mineral foliation, defined by alkali feldspar, is oblique to the modal layering (Fig. 6b, d). To the SE of a large naujaite outcrop, the modal layers have a bowl-like form dipping *c.* 25° SE in the west and *c.* 15° NW in the east (Fig. 6a). Along the Kringlerne cliff, the modal layers are roughly planar, dipping *c.* 13° towards the north and, at locality 1, the layers dip 39° towards the NE (Fig. 6b, d). Unit +3 contains roof rock autoliths within its white layer, deflecting the modal layers both above and below (Fig. 6c).

A mineral foliation defined by alkali feldspar is present across the kakortokites (Figs 6b, 7, 8c, d); the alkali feldspar typically has a tabular habit with occasional kinking observed in the black and white layers (Fig. 8a, b). Kinking of alkali feldspar mostly occurs where cumulus alkali feldspar grains are tightly packed with the grains abutting one another. The degree of alkali feldspar alignment varies through the layers, appearing weakest in the centre of the red layers and strongest in the black layers (Fig. 7). The degree of mineral alignment of the alkali feldspar within the white layers is variable (Fig. 7). The mineral foliation defined by alkali feldspar is often oblique in both strike and dip to the modal layering and cross-cuts the modal layer boundaries; this obliquity was observed in the NE of the kakortokites (Fig. 6b, d). The obliquity between the strike of the mineral foliation and the modal layering ranges from *c.* 10° to *c.* 45°;

the strike of the mineral foliations and modal layering are typically SW-NE or NW-SE (Fig. 6b, d). The modal layering typically dips more steeply than the mineral foliation, with the degree of obliquity ranging from sub-parallel to *c.* 35° (Fig. 6b, d). At locality 2, the mineral foliation is slightly steeper than the modal layering by *c.* 10°. One mineral lineation defined by arfvedsonite was observed in the field at locality 2; the lineation (27°→311) is near-parallel to the strike of the mineral foliation (341/19° NE) and trends in the dip direction of the modal layering (220/13° NW) (Figs 6d, 8g).

Geological log sections show that layers -1W, 0B, 0R, 0W and +1B at localities 1 and 2 have remarkably similar grain size variations and mineral textures (Fig. 7). The thickness of the layers varies between units, with the white layers often three to five times thicker than the black and red layers; the black and red layers typically vary from 0.5 to 2 m thick, whereas the white layers typically range from 3 to 10 m thick (Figs 1c, 7).

Centimetre-scale layering within the kakortokites was also observed with more varied modal compositions and no consistency with regards to layer thickness (Fig. 8l). Layer -1W consists of densely packed, large (*c.* 1 cm) cumulus alkali feldspar laths with mainly intercumulus arfvedsonite (Figs 7, 8b). The transition from layer -1W to layer 0B is relatively sharp, occurring over 1 cm; at locality 1 an aegirine vein *c.* 1 cm wide follows the contact of the modal layering (Figs 6b, 7). In addition to the aegirine vein at locality 1, aegirine is present in minor quantities through the layers, typically *c.* 1% modal abundance; aenigmatite is also present in minor quantities <1% (Fig. 7). Layer 0B fines upwards and consists mostly of fine-grained cumulus arfvedsonite between strongly aligned 0.5–

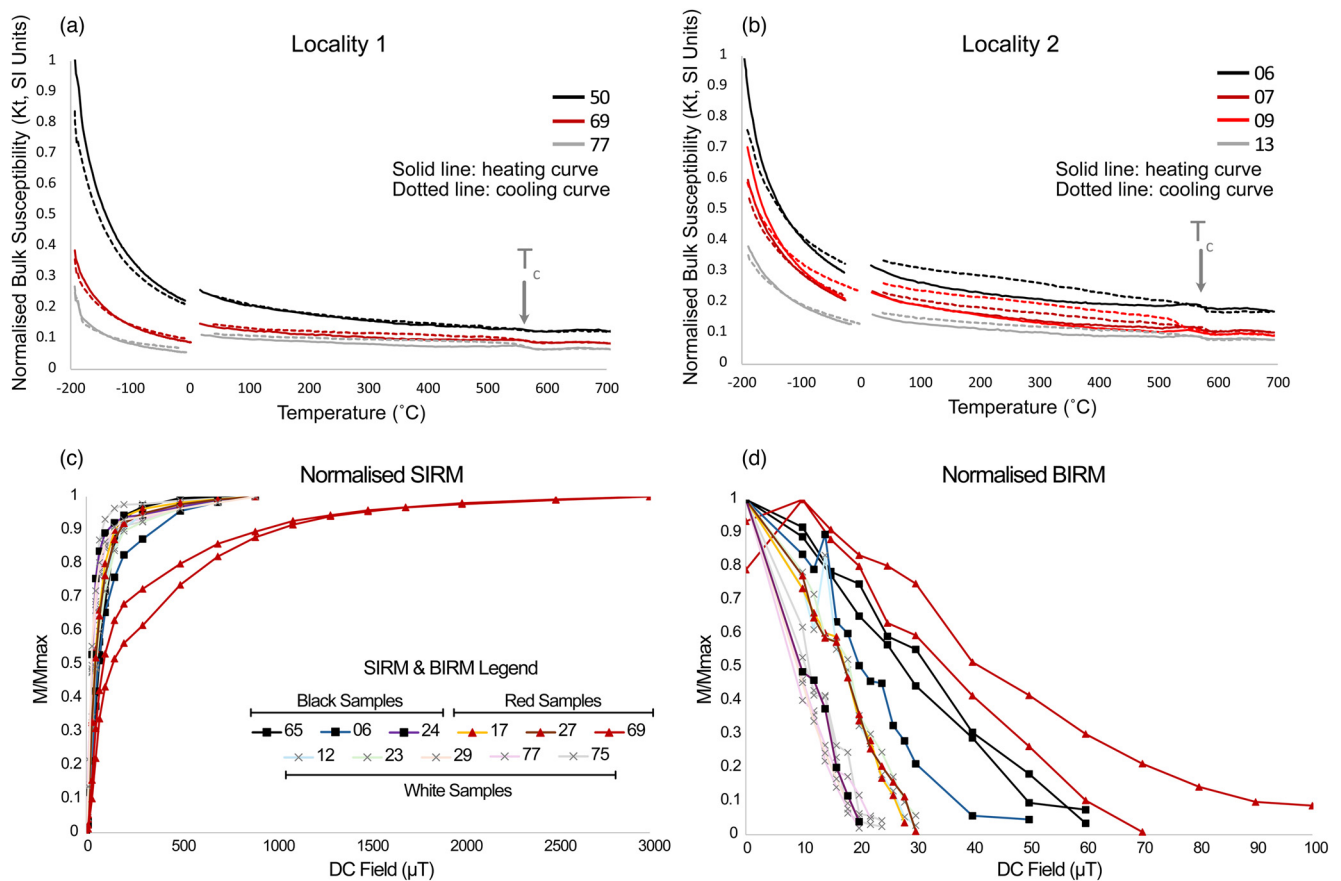


Fig. 9. (a) Results of temperature susceptibility experiments from locality 1, coloured black, red and white to correspond with the colour layer the sample is from. (b) Results of temperature susceptibility experiments from locality 2. (c) Saturation isothermal remanent magnetization results and (d) back-field isothermal remanent magnetization results. Duplicate experiments were run on samples 65, 69, 75 and 77. BIRM, back-field isothermal remanent magnetization; SIRM, saturation isothermal remanent magnetization.

1 cm cumulus alkali feldspar laths (Figs 7, 8d). The arfvedsonite within layer 0B often has irregular, patchy zoning and sometimes has a granular texture (Fig. 8k; Supplementary Material).

The transition from layer 0B to layer 0R is gradual over 10 cm (Figs 4a, 7). Layer 0R coarsens upwards and has densely packed cumulus eudialyte and alkali feldspar with intercumulus arfvedsonite at its base, which becomes oikocrystic surrounding nepheline upwards through the layer (Fig. 7). Patchy alteration of alkali feldspar, nepheline and eudialyte is associated with white veining present within layer 0R at locality 1 (Fig. 7).

The transition from layer 0R to layer 0W occurs gradually over 20–30 cm (Fig. 7). The base of layer 0W is dominated by a finer grained (<5 mm) intercumulus nepheline groundmass with larger (c. 1 cm) cumulus alkali feldspar laths (Figs 7, 8e, j). Arfvedsonite occurs as large (1–2 cm) oikocrysts containing nepheline; irregular, wavy grain boundaries are present around the nepheline, indicative of disequilibrium between the nepheline and arfvedsonite (Figs 7, 8e, f). Roughly halfway through layer 0W, arfvedsonite is no longer oikocrystic and becomes cumulus and intercumulus between densely packed cumulus alkali feldspar laths (Fig. 7).

Layers +1B and +1R are poorly defined with a gradual transition between the two occurring over 10 cm; these layers contain coarse-grained cumulus c. 1 cm arfvedsonite with minor amounts of intercumulus arfvedsonite (Fig. 7). Layer +1W fines upwards and consists of densely packed cumulus alkali feldspar laths; arfvedsonite is mostly cumulus throughout the layer (Fig. 7). Layers +2B, +2R and +2W are remarkably similar to layers +1B, +1R and +1W (Fig. 7). A common feature across all the layers is that intercumulus arfvedsonite often replaces areas of cumulus alkali feldspar (Fig. 8b, i).

Rock magnetic characterization

The temperature susceptibility results show a strong consistency across the samples, with the Curie temperatures (T_c), the temperature above which ferromagnetic minerals behave paramagnetically, ranging from 560 to 580°C (Fig. 9a, b). A strong exponential decrease in susceptibility is observed between –194 and 400°C, with another decrease in susceptibility occurring around 580°C. These results indicate a large paramagnetic contribution, and a minor contribution from magnetite, to the magnetic susceptibility at room temperature (Dunlop and Özdemir 1997).

With the exception of sample 69, all the black, red and white samples reach magnetic saturation ($M/M_0 > 0.95$) between 150 and 300 mT (Fig. 9c). Sample 69 reaches magnetic saturation at 1500 mT, significantly higher than the rest of the samples (Fig. 9c). The BIRM curves show that all the samples have relatively low remanence coercivity. With the exception of sample 69, the white samples have the lowest coercivity, followed by the red and then black samples (Fig. 9d). Samples that are easily magnetically saturated with low coercivity indicate the presence of magnetite (Dunlop and Özdemir 1997). The higher magnetic saturation and coercivity of sample 69 are indicative of a different mineral phase being present, such as maghemite (Dunlop and Özdemir 1997).

Magnetic susceptibility and anisotropy results

Magnetic parameters

K_{mean} , P_j and T display clear patterns that coincide with the logged mineral and textural changes through the layered sequence (Fig. 10). The K_{mean} values range from 2.09×10^{-3} to 2.67×10^{-4} SI, with the

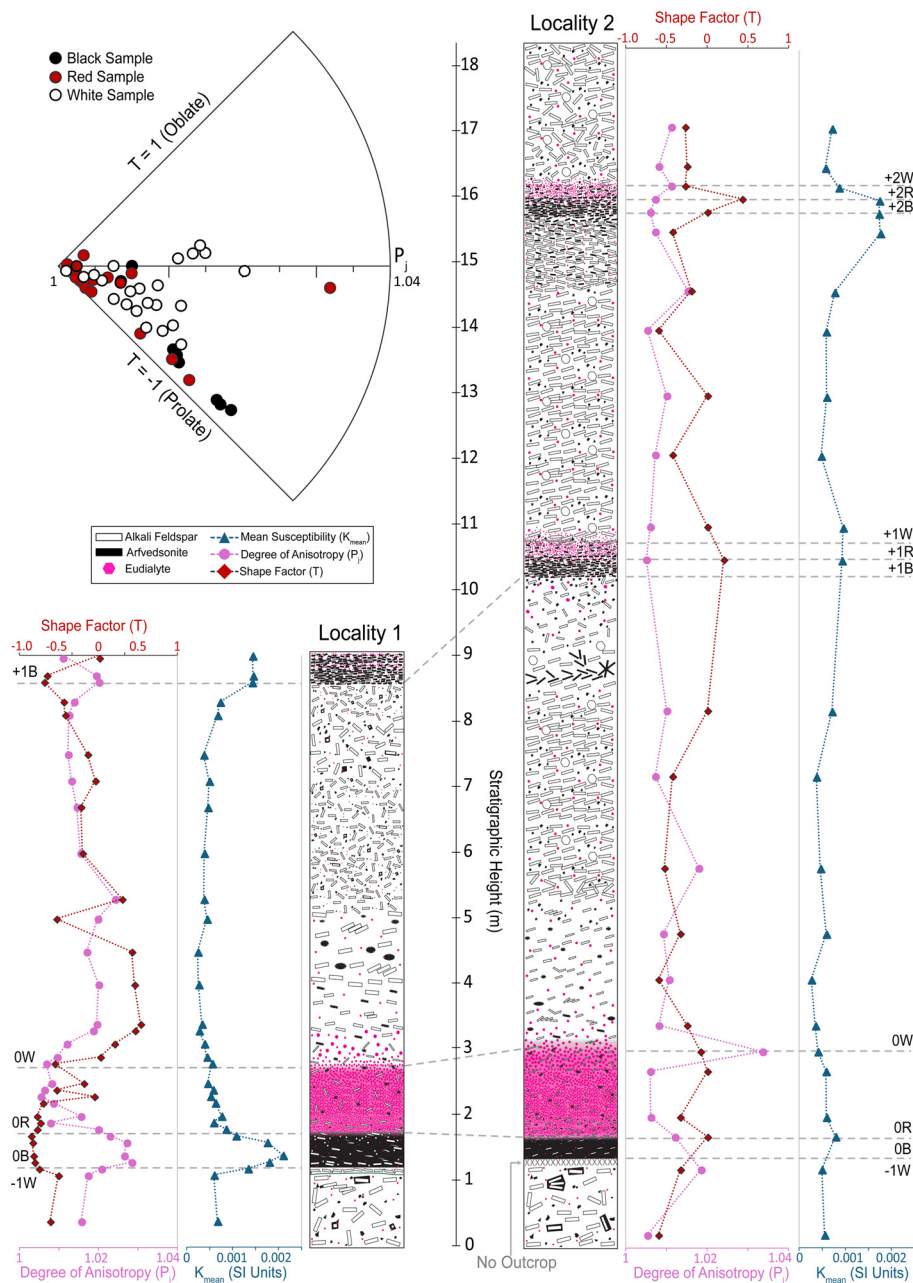


Fig. 10. Stratigraphic logs for locality 1 (left-hand panel) and locality 2 (right-hand panel). Plotted adjacent to the logs are the mean susceptibility (K_{mean}) in blue, the anisotropy of magnetic susceptibility degree of anisotropy (P_j) in pink and the anisotropy of magnetic susceptibility shape factor (T) in red. Top left: T v. P_j polar plot, with each point representing the average T and P_j data from a sample site. All sample sites from both localities are plotted.

highest K_{mean} values in the samples with the highest arfvedsonite content and a steady decrease in K_{mean} as the arfvedsonite content decreases (Fig. 10). The degree of anisotropy (P_j) ranges from 1.038 to 1.006, with the strongest P_j values typically occurring in the black layers and at the layer transitions (Fig. 10). The shape factor (T , Fig. 4b) values range from -0.89 to 0.43 , with almost all samples plotting in the prolate field; the black samples have the most prolate fabrics (Fig. 10). The K_{rem} values, the K_{mean} of the AARM data, range from 7.16×10^{-5} to 5.35×10^{-4} SI, with no clear pattern observed between K_{rem} and mineral modal abundances.

AMS and AARM data

The AMS data across both outcrops consistently display a subvertical K_1 with a sub-horizontal K_2 and K_3 ; all three susceptibility axes have well-constrained 95% confidence ellipses across all sample sites, indicating that both a magnetic foliation and lineation are present (Fig. 11). While K_1 remains consistently subvertical across the dataset, the orientation of K_2 and K_3 rotates anticlockwise from the SE towards the NE as the mineral mode varies across the layers (Fig. 11, stereonet A). Samples that contain more arfvedsonite (i.e. the black

layers) have a K_3 that plots towards the NE and, as the arfvedsonite content decreases (i.e. the red and white layers), K_3 tends to plot towards the SE (Fig. 11, stereonet A). At locality 2, the plane to K_1 is near-parallel to the field-measured modal layering, except for sample 17 from layer +1B (Fig. 11). At locality 1, the plane to K_1 is consistently oblique to the modal layering, with the plane to K_1 recording a near-horizontal dip, whereas the modal layering dips 39° .

The AARM data display two main trends: samples that have a NE–SW-striking ferromagnetic foliation plane and samples that have an NW–SE-striking ferromagnetic foliation plane (Fig. 11). The samples that have NE–SW-striking AARM foliations are from the red and white layers (samples 06, 23, 29, 69 and 77), whereas those that have NW–SE-striking AARM foliations are from the black layers and the white layers containing oikocrystic arfvedsonite (samples 12, 17, 24, 27, 50, 75 and 85; Fig. 11). All the AARM foliations are highly oblique to orthogonal to the modal layering (Fig. 11). The AARM strike is nearly perpendicular to the modal layering in most samples and the difference in dip between the AARM foliation and the modal layering ranges from near-parallel to $c. 90^\circ$ (Fig. 11). The AARM data also show a consistent magnetic lineation (R_1) that is well-defined and typically lies along the

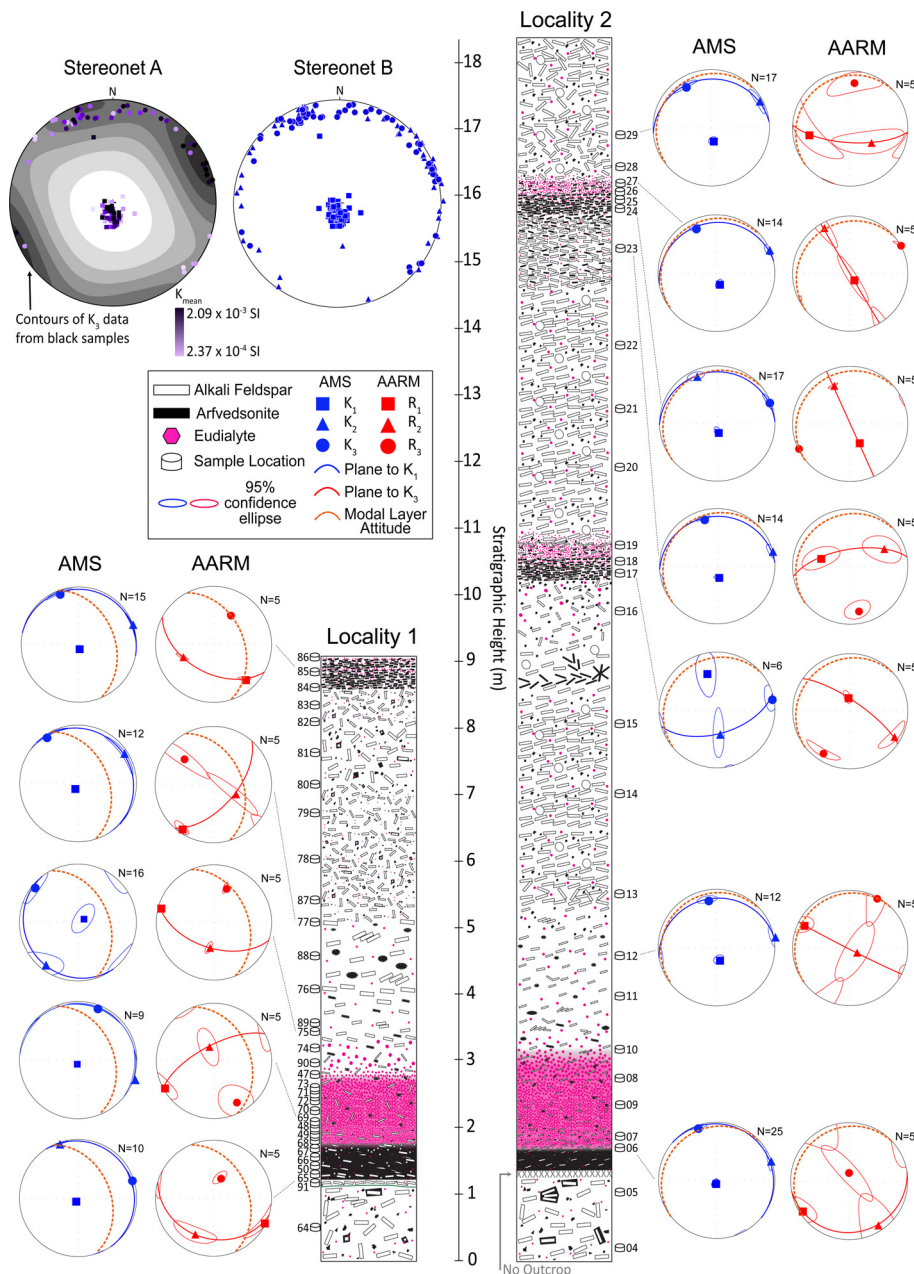


Fig. 11. Anisotropy of magnetic susceptibility and anisotropy of anhysteretic remanence data from locality 1 (left-hand panel) and locality 2 (right-hand panel), where N is the number of sub-specimens analysed per sample site. Stereonet A: average K_1 and K_3 data from each sample site at both localities, coloured by mean susceptibility. The contours are the K_3 data from the black samples, showing that in the black layers K_3 is typically oriented towards the NE. A progressive rotation of K_3 from NE to SE is observed as the mean susceptibility decreases. Stereonet B: average K_1 , K_2 and K_3 data from each sample site at both localities. AARM, anisotropy of anhysteretic remanence; AMS, anisotropy of magnetic susceptibility.

igneous layering plane (Fig. 11). The orientation of the AARM R_1 maintains a coaxial relationship with the orientation of the AMS K_2 ; this correlation is strongest in the white layers and weakest in the black layers (Fig. 11). In brief, the AARM suggests there is a ferromagnetic foliation that is orthogonal to the modal layering with a consistent lineation along the modal layering plane.

CPO

CPO was completed on samples 65 (60% modal arfvedsonite), 69 (20% modal arfvedsonite) and 77 (10% modal arfvedsonite) from the black, red and white layers of unit 0 at locality 1, and on sample 24 (65% modal arfvedsonite) from layer +2B at locality 2 (Figs 4b, 7). Arfvedsonite exhibits varying degrees of mineral alignment, as observed in the CPO pole figures across the samples; a marked decrease in CPO is recorded in sample 77 with 10% modal arfvedsonite (Fig. 12). In sample 65 (layer 0B), the arfvedsonite shows a CPO with the (110) poles girdling a sub-horizontal plane and the (001) poles normal to the sub-horizontal plane (Fig. 12). Sample 69 (layer 0R) shows a similar CPO to sample 65; a weak alignment of the (010) poles is also apparent in the NW quadrant of

the stereonet (Fig. 12). In sample 24 (layer +2B), the arfvedsonite (010) poles are normal to the sub-horizontal plane, with the (001) poles girdling the sub-horizontal plane; this CPO is orthogonal to the arfvedsonite CPO in sample 65 (layer 0B) (Fig. 12). No clear CPO is observed in sample 77 (layer 0W). Alkali feldspar records a high degree of CPO across all samples; the (100) and (001) poles girdle a sub-horizontal plane and the (010) poles are normal to the sub-horizontal plane (Fig. 12).

Eudialyte records a clear CPO in samples 69 and 77 (Fig. 12). In sample 69 (0001), the poles cluster in the NE quadrant, with the (10–10) and (11–20) poles girdling a NW–SE plane dipping $c. 40^\circ$ SW (Fig. 12). Sample 77 records a eudialyte CPO orthogonal to sample 69; the (0001) poles cluster in the SW quadrant, with the (10–10) and (11–20) poles girdling a NW–SE plane dipping $c. 40^\circ$ NE (Fig. 12). No clear eudialyte CPO is recorded in samples 65 or 24 (Fig. 12).

Nepheline records a high degree of CPO in samples from unit 0; in samples 69 and 77 the (0001) poles cluster in the SW quadrant and the (10–10) poles girdle a NW–SE plane dipping $c. 40^\circ$ SE (Fig. 12). In sample 65, the nepheline CPO is orthogonal to the other samples, with the (0001) poles clustering in the NE quadrant and the

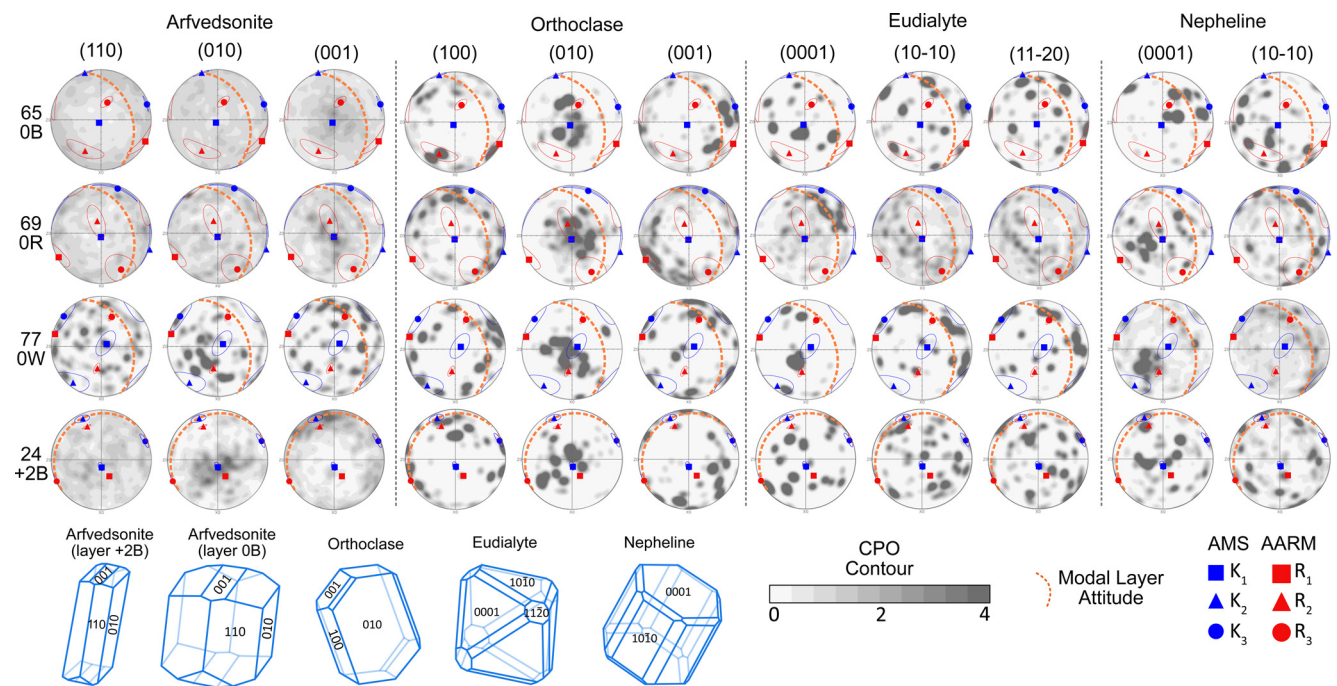


Fig. 12. Results of electron back-scatter diffraction, anisotropy of magnetic susceptibility and anisotropy of anhysteretic remanence on representative samples from layers 0B (sample 65), 0R (sample 69) and 0W (sample 77) from unit 0 and layer +2B (sample 24). The electron back-scatter diffraction data are plotted as pole figures of the relevant crystal planes for the main cumulus and intercumulus minerals in the kakortokites. The electron back-scatter diffraction pole figures are plotted in the ZX plane, displayed as equal-area stereonets in the lower hemisphere and reoriented to the geographical coordinate system for direct comparison with the anisotropy of magnetic susceptibility and anisotropy of anhysteretic remanence data. The crystallographic preferred orientation contour indicates multiples of random distribution. The modal layering attitude as measured in the field is displayed on each pole figure (orange plane). Schematic crystal shapes with the crystallographic preferred orientation faces labelled are displayed at the base of the figure (these may not match the habits of the euhedral crystals that were present in the magma). AARM, anisotropy of anhysteretic remanence; AMS, anisotropy of magnetic susceptibility; CPO, crystallographic preferred orientation.

(10–10) poles girdling a NW–SE plane dipping *c.* 40° SW. A weak eudialyte CPO is recorded in sample 24, where the (10–10) poles girdle a sub-horizontal plane and the (0001) poles are normal to the sub-horizontal plane (Fig. 12). It is noted that both eudialyte and nepheline have near-isotropic crystal morphologies and therefore, although the CPO is consistent, the shape-preferred orientation of the minerals may not be.

Comparison of the field-observed modal layering, CPO and magnetic fabric

In unit 0, the sub-horizontal girdling of the arfvedsonite (110) poles and the alkali feldspar (100) and (001) poles are typically shallower than the igneous layering by *c.* 20° (Fig. 12). The girdling of the eudialyte (10–10) and (11–20) poles and the nepheline (10–10) poles are typically parallel to the igneous layering (Fig. 12). In layer +2B, the sub-horizontal girdling of the arfvedsonite (001) poles, the alkali feldspar (100) and (001) poles and the (10–10) poles are all near-parallel to the igneous layering (Fig. 12). All the minerals record a weak correlation between the grouping of the poles to the crystal planes and the orientation of the AARM axes (Fig. 12). Across all the mineral phases, the AARM axes correspond to varying poles to crystal planes (i.e. there is no consistent relationship between the specific AARM axes and the poles to crystal planes).

The arfvedsonite CPO in samples 65 and 69 corresponds well to the AMS axes; there is a grouping of the (001) poles with the AMS K_1 and the (110) poles with the AMS K_3 (Fig. 12). Sample 69 also records a grouping between the arfvedsonite (010) poles and the AMS K_2 (Fig. 12). The arfvedsonite CPO in sample 24 also corresponds well to the AMS axes with the (010) poles grouping with the AMS K_1 and the (001) poles grouping with the AMS K_2

(Fig. 12). Across all samples, the alkali feldspar CPO corresponds to the AMS axes: the (010) poles are coaxial with the AMS K_1 , the (100) poles are coaxial with the AMS K_2 and the (001) poles are coaxial with the AMS K_3 . The eudialyte and nepheline CPOs do not show a clear relationship with the AMS axes (Fig. 12).

Discussion

Relationship between petrofabrics and magnetic fabrics

To identify the minerals that contribute to and dominate the magnetic fabrics recorded through the layers of the kakortokites at Ilimaussaq, we first identify the magnetic mineralogy of the rocks and then relate the measured magnetic fabrics with the silicate mineral fabrics identified in the field and through CPO analysis. By doing this, we create a robust textural context of the layers allowing for the interrogation of previously proposed open and closed system layering hypotheses, which cite differing physical magmatic processes that should be recorded in the rock record (Fig. 3).

Magnetic mineralogy

The kakortokites largely (25–75%) consist of diamagnetic minerals, such as alkali feldspar and nepheline. Diamagnetic mineral phases have weak magnetic susceptibilities (typically *c.* 1×10^{-6} SI) so are expected to make a negligible magnetic contribution to the kakortokites (e.g. Tarling and Hrouda 1993; Rosenblum and Brownfield 2000; O'Driscoll *et al.* 2008; Biedermann *et al.* 2016). Eudialyte has an isotropic morphology across all the samples and therefore is also unlikely to significantly contribute to the magnetic fabrics (O'Driscoll *et al.* 2024).

By contrast, paramagnetic minerals, such as amphibole and pyroxene, typically have bulk magnetic susceptibility values of $c. 1 \times 10^{-4}$ SI (Borradaile *et al.* 1987). Given that the K_{mean} values of our samples are $>2.4 \times 10^{-4}$ SI, and the strong exponential decrease in susceptibility from -190 to 400°C observed in temperature susceptibility experiments at both study sites (Fig. 9a, b), the paramagnetic minerals likely make a substantial/dominant contribution to the bulk magnetic susceptibility. In our samples, the paramagnetic phases arfvedsonite, aegirine and aenigmatite are all present (Fig. 7) (Rosenblum and Brownfield 2000). Aenigmatite occurs in $c. 1\%$ modal abundance, so likely does not contribute significantly to the bulk magnetic susceptibility. Aegirine occurs in $c. 1\%$ modal abundance across most layers, with its highest abundance reaching $c. 5\text{--}10\%$ in layer 0W at locality 2. O'Driscoll *et al.* (2024) found that the aegirine at Ilimaussaq has a much lower theoretical bulk susceptibility than arfvedsonite; given this and its low modal abundance, aegirine likely does not contribute significantly to the bulk susceptibility. Arfvedsonite occurs in $10\text{--}60\%$ modal abundance and therefore is determined to be the dominant carrier of magnetic susceptibility. A clear relationship between the bulk magnetic susceptibility and arfvedsonite abundance is observed at both localities 1 and 2, where the arfvedsonite-rich ($>55\%$) black layers have the highest K_{mean} values (9.26×10^{-4} to 2.09×10^{-3} SI) and the arfvedsonite-poor ($<30\%$) white layers have the lowest K_{mean} values (2.37×10^{-4} to 9.50×10^{-4} SI) (Fig. 10); these observations further substantiate the interpretation that arfvedsonite dominates the bulk magnetic susceptibility.

In addition to the paramagnetic component, our rock magnetic analyses show that all the samples contain a mineral phase that carries remanence, a feature unique to ferromagnetic and anti-ferromagnetic minerals (Figs 9c, d and 11) (e.g. Tarling and Hrouda 1993). All the samples, except sample 69, reach 95% magnetic saturation in isothermal remanent magnetization fields below 200 mT and exhibit a $c. 560\text{--}580^\circ\text{C}$ Curie temperature (Fig. 9a–c); these characteristics are consistent with the presence of magnetite (Dunlop and Özdemir 1997). We did not observe any magnetite in our thin sections or when using a scanning electron microscope, but note that magnetite can be $<1\text{ }\mu\text{m}$ and occurs in very low abundance in these samples, making it undetectable using these methods (Dunlop and Özdemir 1997).

Sample 69 from layer 0R has a deep red discoloration and requires isothermal remanent magnetization fields >1.5 T to reach 95% saturation, which could indicate the presence of maghemite (Fig. 9c) (Dunlop and Özdemir 1997). Maghemite is known to form via the partial oxidation of magnetite during hydrothermal alteration (Dunlop and Özdemir 1997). Late-stage alteration associated with white veins cross-cutting the kakortokites was observed in the field at layer 0R (Fig. 7), supporting the interpretation that maghemite is a product of late-stage hydrothermal alteration. We did not observe any maghemite in our thin sections or when using a scanning electron microscope; however, samples with minimal alteration were selected for the thin section analyses, which may explain why we did not observe it.

In summary, the main magnetic minerals within the kakortokites are arfvedsonite and magnetite. The bulk magnetic susceptibility is dominated by the paramagnetic contribution from arfvedsonite, with a minor ferromagnetic contribution from magnetite.

Carriers of AMS

If a rock contains ferromagnetic minerals and $>10\%$ paramagnetic minerals, as is the case for the kakortokites (Fig. 7), both the paramagnetic and ferromagnetic minerals contribute to the AMS fabric (i.e. the orientation of the magnetic fabric) (Tarling and Hrouda 1993). Although arfvedsonite ($10\text{--}60\%$ modal abundance) is more abundant than magnetite (likely much less than 1% modal

abundance) within our samples, previous studies have shown that magnetite may dominate AMS fabrics even if present in trace amounts (e.g. Borradaile 1987, 1988; Clark 1997; Biedermann *et al.* 2015a; Parés 2015; Ageeva *et al.* 2017, 2020). Therefore, to interpret the magnetic fabric, we must first determine whether arfvedsonite or magnetite dominates the AMS.

The CPO data provide valuable insights into the relationship between the silicate petrofabric defined by arfvedsonite and the magnetic fabrics. The correlation between the AMS axes and CPO poles to the arfvedsonite crystal planes weakens as the arfvedsonite content decreases (e.g. compare the arfvedsonite CPO from sample 65 with that of sample 77, Fig. 12). By contrast, the AARM axes, which only represent the ferromagnetic component of the samples, maintain a correlation with the poles to the crystal planes in all samples (Fig. 12). The grouping of the AARM data with the CPO poles of all minerals suggests that magnetite could be present as small ($<1\text{ }\mu\text{m}$) exsolved minerals within the silicate phases or present interstitially in orientations controlled by the silicate minerals. Therefore, although the paramagnetic component is recording the sub-horizontal foliation of arfvedsonite (Fig. 12), the ferromagnetic component defined by magnetite is recording a foliation normal to the igneous layering. These two conflicting mineral fabrics, defined by arfvedsonite and magnetite, will both contribute to the AMS (Tarling and Hrouda 1993).

Systematic variations in the contribution of the paramagnetic and ferromagnetic components to the AMS correlate with the changes in mineral abundance within the samples (Fig. 11, stereonet A). Specifically, the samples with higher magnetic susceptibility values of $c. 1 \times 10^{-3}$ SI (black layers) typically have AMS K_3 (i.e. the pole to the magnetic foliation) plunging $c. 10^\circ$ to the NE, whereas samples with lower magnetic susceptibility values $c. 1 \times 10^{-4}$ SI (white layers) typically have an AMS K_3 plunging $c. 10^\circ$ to the SE (Fig. 11, stereonet A). This NE–SE rotation of the AMS fabric is not recorded in the silicate fabric in the field or the CPO data, suggesting that the rotation could be due to competing paramagnetic and ferromagnetic fabrics. For example, the AARM R_1 and AMS K_2 have a weak correlation in the black layers and a stronger correlation in the white layers (Fig. 11). We suggest that this is evidence of the ferromagnetic contribution influencing the orientation of the AMS axes, causing the rotation of K_3 towards the SE when the arfvedsonite abundance is low. Alternatively, the rotation of the AMS fabric may be due to changes in arfvedsonite chemistry. Lindhuber *et al.* (2015) recorded significant variability in arfvedsonite chemistry in the white layers compared with the black layers. This variation in mineral chemistry through the stratigraphic section could affect the AMS fabric (Biedermann *et al.* 2015a).

In summary, arfvedsonite dominates the AMS when it is present in high modal abundance in the black kakortokite layers, whereas magnetite may contribute a proportionally larger amount to the AMS in the white layers with a low arfvedsonite modal abundance. This interpretation is consistent with other layered intrusion studies that also found that the AMS varies in response to contributions by competing mineral fabrics (Maes *et al.* 2008; Ferré *et al.* 2009, 2012; Biedermann *et al.* 2016). The magnetite contribution is likely to be small and the variations observed in the AMS fabric orientation may also be explained by changes in arfvedsonite chemistry. Given the variability in the orientation of the AMS fabric, care should be taken when interpreting the fabrics, particularly the orientation of the magnetic lineation.

Magnetic and silicate mineral fabric data in the context of field relationships

Both the AARM and AMS data maintain a consistent relationship relative to the macroscopic silicate fabrics (Fig. 12). The AARM ferromagnetic fabric is highly oblique to orthogonal to the modal

layering, recording a subvertical foliation defined by magnetite (Fig. 11). In our AMS data, K_1 is consistently orthogonal to the silicate mineral foliation of arfvedsonite and alkali feldspar (Fig. 12) – that is, the AMS fabric is inverse to the silicate mineral fabric, such that the AMS K_1 records the pole to the mineral foliation, whereas either the AMS K_2 or K_3 records the mineral lineation (see Ferré 2002). Similar inverse fabrics have been identified in previous studies in minerals such as single-domain magnetite, hematite, tourmaline and amphibole (Borradaile and Henry 1997; Borradaile and Gauthier 2001; Ferré 2002; Biedermann *et al.* 2015a, 2018; O'Driscoll *et al.* 2024). We note that although our AMS K_1 is consistently orthogonal to the silicate mineral foliation, the AMS K_1 is coaxial with the arfvedsonite (001) poles in layer 0B and coaxial with the arfvedsonite (010) poles in layer +2B (Fig. 12). This relationship is in line with previous work completed on amphibole-bearing rocks, where samples with a differing CPO (e.g. a girdle v. point distribution of the crystallographic axes) produce similar AMS orientations (Biedermann *et al.* 2018). Given our inverse AMS results, the subvertical AMS K_1 axes are attributed to the occurrence of a consistent sub-horizontal mineral foliation through all the igneous layers (Fig. 11). The sub-horizontal mineral foliation is near-parallel to the modal layering at locality 2, but oblique to the modal layering at locality 1 and the surrounding area (Figs 6b, d and 11).

Well-constrained 95% confidence ellipses around the AMS K_2 and K_3 suggest that a mineral lineation is also present throughout the layers, although we cannot definitively determine which of K_2 or K_3 record the crystal long axes (Fig. 11). The presence of mineral lineations is supported by the observation of an arfvedsonite lineation in the field at locality 2 (Figs 6d, 8g). At locality 1, the AMS K_2 and K_3 are oblique to the layering; however, at locality 2, the AMS K_2 or K_3 coincide with the dip azimuth or the strike of the modal layering. This suggests that there is a mineral lineation oriented within the modal layering at locality 2, whereas at locality 1 there is a mineral lineation oblique to the modal layering (Fig. 11).

Testing layering models using magnetic and crystal fabric data

To interpret our fabric data within the kakortokites, we must first establish whether the fabrics are primary magmatic or a tectonic overprint. Regional sinistral transcurrent faulting was potentially active during and after the emplacement of the Ilímaussaq complex (Chadwick and Garde 1996; Upton 2013). Post-magmatic overprinting would likely result in the re-alignment of the earlier fabrics with the wider tectonic stress field or local deformation zones (Benn *et al.* 1998; Žák *et al.* 2005; McCarthy *et al.* 2015; Burton-Johnson *et al.* 2019; Latimer *et al.* 2024). The orientation of the mineral foliations and lineations are highly oblique to the previously proposed strike-slip faulting; zones of concentrated subvertical shearing were not observed in the outcrops visited in this study (Fig. 7). Evidence of brittle deformation was not identified within the kakortokites; however, the occasional kinking of alkali feldspar suggests that some dynamic recrystallization occurred (Figs 7, 8b). The fabrics observed in the kakortokites are therefore considered to be magmatic in origin rather than a post-magmatic tectonic overprint. The fabrics within the kakortokites therefore represent only the magmatic state and crystal mush processes.

Having established that the fabrics we record are likely magmatic, we now examine how they compare with previous layering hypotheses. The open system model invokes *in situ* crystallization for the black and red layers, and gravitational settling within the white layers (Hunt *et al.* 2017). The change from *in situ* crystallization to gravitational settling should result in the white layers having the strongest mineral foliations, whereas the black

and red layers should have the weakest or no fabric (Figs 2a, 3) (Meurer and Boudreau 1998). This is inconsistent with our data, which show that the strongest mineral alignment is within the black layers (Figs 7, 10).

Additionally, in the open system model, compaction of the crystal pile is used to explain all the foliations in the layers across kilometres of the intrusion (Hunt *et al.* 2017). Although compaction may cause the reorientation of crystals within a mush, it is debatable how effective compaction is at forming consistent, well-defined foliations, making it a questionable sole source of the foliations observed in the kakortokites (Higgins 1991; Meurer and Boudreau 1998; Holness *et al.* 2017; Bachmann and Huber 2019; Kruger and Latypov 2022). The oblique relationship between the mineral foliation and the modal layering observed in our data (Fig. 6b) is also difficult to reconcile with an open system model (Fig. 2a). If a primitive magma were to be injected over the crystal pile to form a new black layer, it would likely erode, disrupt and/or form a new fabric at the layer boundary. This is inconsistent with our observations showing that the foliation defined by alkali feldspar cross-cuts the –1W/0B modal layering boundary, maintaining continuity irrespective of the layer change (Fig. 6b). We therefore suggest that the crystal size distribution data in Hunt *et al.* (2017), which is indicative of *in situ* nucleation and crystal growth, largely reflects post-accumulation textural coarsening of the crystal pile. This is supported by significant overgrowths making up 10–50% of eudialyte, as recorded by Borst *et al.* (2018), and the partially granular texture of layer 0B observed in thin section, which has curvilinear grain boundaries and 120° three-grain junctions (Fig. 8i, k; Supplementary Material).

In the closed system model, the gravitational settling of crystals would be expected to produce foliations across entire igneous layers (Figs 2b, 3b). This is consistent with our data, which records continuous sub-horizontal mineral foliations through the layers (Fig. 11) (Meurer and Boudreau 1998). The closed system model also suggests that arfvedsonite and alkali feldspar mats form simultaneously, with the alkali feldspar mats becoming trapped beneath the arfvedsonite mats (Bons *et al.* 2015; Lindhuber *et al.* 2015). The contemporaneous formation of adjacent black and white layers is supported by our observation of a continuous alkali feldspar foliation across layer boundaries (Fig. 6b).

The quasi-closed mush compartments proposed in the closed system model may also be supported by the difference in arfvedsonite shape and CPO between the layers in unit 0 and layer +2B (Fig. 12). In layer +2B, we observe elongate arfvedsonite crystals that define a sub-horizontal foliation (Fig. 8g, h); however, in layer 0B, the arfvedsonite crystals are observed as a stubby groundmass (Fig. 8a, d, i; Supplementary Material). The difference in arfvedsonite crystal shape between layers +2B and 0B coincides with a change in the arfvedsonite CPO (Fig. 12). In layer +2B, the arfvedsonite (010) poles are subvertical and normal to the silicate foliation, whereas in layer 0B the arfvedsonite (001) poles are subvertical and normal to the silicate foliation (Fig. 12). As arfvedsonite is typically elongate along [001] (Gordon 1927; Hogarth *et al.* 1987), we would generally expect sub-horizontal (001) poles and subvertical (010) poles normal to the silicate foliation, as is recorded in layer +2B (Fig. 12). We suggest that the arfvedsonite crystal habit may vary between the layered units and that it perhaps has a stubby habit in layer 0B, but a more elongate habit in layer +2B (see idealized crystal shapes, Fig. 12).

Although few studies have investigated changes in amphibole habit, work on feldspars has shown that their habit varies between prismatic and tabular with changes in cooling rate (Holness 2014) or the degree of under-cooling (Mangler *et al.* 2022). Recent amphibole crystallization experiments from crushed basalt samples revealed crystal shape and size differences with changes in temperature, pressure and crystallization time (Zhang *et al.* 2019).

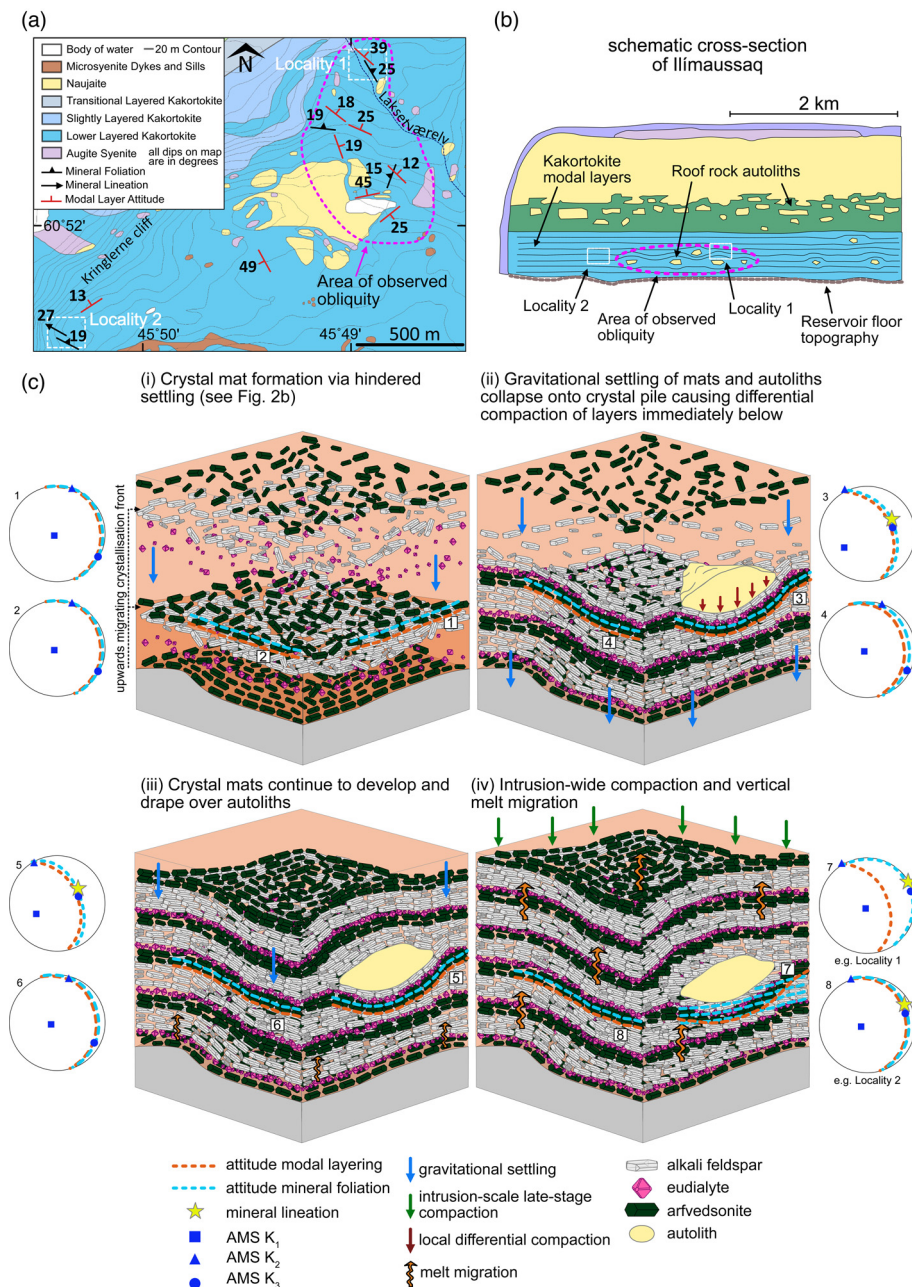


Fig. 13. (a) Structural map of the kakortokites showing where obliquity between the mineral foliation and the modal layering is recorded. (b) Schematic cross-section of Ilimaussaq. (c) Crystal mat model showing stages of development and the predicted mineral and magnetic fabrics that would be produced. Source: geological map in part (a) modified after Andersen *et al.* (1988) and Upton (2013); part (b) adapted from Andersen *et al.* (1981) with proposed locations of our study localities marked. AMS, anisotropy of magnetic susceptibility.

The shape of amphiboles varies from bladed to prismatic with increasing temperature or time, and from bladed to tabular with increasing pressure, suggesting that, like feldspar, amphibole habits are sensitive to the magmatic conditions (Zhang *et al.* 2019). If arfvedsonite crystals have a stubby morphology, gravitational settling of the crystals would form sub-horizontal foliations along the (001) crystal faces, as recorded in layer 0B (Fig. 12). By contrast, gravitational settling of acicular arfvedsonite elongate along [001] would form foliations along the (010) crystal faces, as recorded in layer +2B (Fig. 12).

The vertical (001) poles in layer 0B may also be explained by *in situ* growth with a vertical chemical or temperature gradient in a process similar to how dendrites or comb layering form (e.g. Lofgren and Donaldson 1975; O'Driscoll *et al.* 2007); however, this would imply that significant heterogeneous nucleation (arfvedsonite nucleating on other arfvedsonite) occurred within layer 0B, which is a thermodynamically unfavourable process (Wieser *et al.* 2019; Holness *et al.* 2023). Overall, we suggest that the changes in arfvedsonite CPO across the layered units likely records variations in arfvedsonite habit due to differences in the magmatic conditions

and subsequent gravitational settling. This suggests that there were slight variations in temperature, pressure and/or chemistry between the layered units, supporting the view that continued gravitational settling occurred within quasi-closed mush compartments (Borst *et al.* 2018).

Although the closed system model explains the recorded mineral foliations within the kakortokites, it does not explain the presence of a lineation through the layers or how the oblique relationship between the mineral foliation and the modal layering formed. Kinked alkali feldspar (Fig. 8b) and the obliquity between the mineral foliation and modal layering (Fig. 6b, d) indicate that a post-cumulus modification process likely occurred (Meurer and Boudreau 1998; Selkin *et al.* 2014). We suggest that two stages of post-cumulus compaction via crystal repacking could explain the lineations and oblique relationships recorded in this study (Fig. 13). To explain the obliquity between the mineral fabric and the modal layering, the area where the obliquity is recorded must be considered. Obliquity is observed in the region at and around locality 1 (Fig. 13a). Notably, this region contains a variety of roof rock autoliths, whereas no large autolith is recorded immediately

around locality 2, where the mineral fabric and modal layering are parallel (Fig. 13a).

In regions with no autolith, the gravitational settling of crystal mats would likely form a sub-horizontal mineral foliation parallel to the modal layering (Fig. 13c (i), c (ii)). Any subsequent pure compaction of these mats would then enhance the pre-existing sub-horizontal foliations. If the gravitational settling and compaction process occurs where the floor of the magma reservoir is inclined, then compaction should have an element of shear to it, producing mineral lineations (Fig. 13c(iv)). We suggest that this is the process we record at locality 2, where the modal layering and mineral foliation are near-parallel and sub-horizontal, and arfvedsonite lineations are present (Figs 8g, 11 and 13c (iv)).

By contrast, areas where autoliths sink onto the crystal pile may instigate differential compaction of the layers immediately below them (Fig. 13c (ii)). Differential compaction due to sinking autoliths may deform previously sub-horizontal layers, causing them to deflect around the shape of the autolith (Fig. 13c (ii)), as we observed in the field (Fig. 6c). At this stage, the mineral foliation may remain parallel to the modal layering (Fig. 13c (ii)). However, as the layers continue to develop, compaction through crystal repacking across the entire crystal pile may occur if the interstitial melt migrates up through the crystal pile (Fig. 13c (iv)).

Crucially, intrusion-wide compaction of the crystal pile may not cause large-scale mineral redistribution, leaving the modal layering attitude unaffected (Fig. 13c (iv)). However, intrusion-wide compaction could flatten pre-existing mineral foliations (Fig. 13c (iv)), particularly foliations defined by elongate minerals (i.e. arfvedsonite and alkali feldspar), through crystal repacking, causing obliquity between the mineral foliation and the modal layering (Figs 6b, 11, 12 and 13c (iv)) (Holness *et al.* 2017; Holness 2018; Bachmann and Huber 2019). Smaller isotropic minerals (i.e. nepheline and eudialyte) likely would not rotate significantly during crystal repacking due to their near-spherical morphology (Bachmann and Huber 2019), explaining why they remain parallel to modal layering as recorded in our CPO data (Fig. 12). We suggest that the vertical migration of melt during compaction is recorded by our subvertical magnetite fabric (Fig. 11), as well as the disequilibrium textures observed in arfvedsonite oikocrysts (Figs 7, 8f).

A closed system model with compaction

In our closed system model, crystal mats form through hindered settling (Fig. 2b) towards the bottom of the magma reservoir (Fig. 13c (i)). The crystal mats continue to develop from the bottom of the magma reservoir up, supported by the upwards fractionation trends through the kakortokites recorded by Borst *et al.* (2018) (Fig. 13c (i)). Continued crystal growth causes the crystal mats to form semi-impermeable mush compartments, isolating melt, which continues to evolve, within them (Fig. 13c (i)) (Bons *et al.* 2015; Lindhuber *et al.* 2015; Borst *et al.* 2018). During the development of the crystal mats, large roof autoliths sink onto the crystal pile (Fig. 13c (ii)). The autoliths locally cause differential compaction of the layers below them; the crystal mats that form after the deposition of the autoliths drape above them (Fig. 13c (ii), (iii)). As the crystal mats continue to develop, the vertical migration of interstitial melt allows compaction via crystal repacking to occur across the intrusion (Fig. 13c (iv)). The continued compaction of the crystal pile does not affect the modal layering attitude, but causes the foliation of elongate minerals, such as arfvedsonite and feldspar, to flatten (Fig. 13c (iv)), creating the obliquity between the mineral foliation and modal layering recorded in field, AMS and CPO data (Figs 6b, d, 11 and 12).

Our data support a closed magmatic system model where igneous layers form through the accumulation of crystal mats. A similar process was invoked to explain the formation of plagioclase and

pyroxene macro-layers within the mafic Skaergaard intrusion (Nielsen *et al.* 2015), suggesting that the magmatic processes recorded in this study are not unique to alkaline intrusions and may be applicable to layered intrusions of varying compositions. Our data also support the interpretation that significant REE deposits are formed from a single major melt injection, which subsequently mechanically self-sorts through gravitational settling to create REE-enriched horizons. Our findings support a growing consensus that petrofabric analyses are powerful tools in deciphering the mechanisms of igneous layering.

Conclusions

Combining field structural relationships, petrography, the CPO and magnetic fabric data has allowed the interrogation of hypothesized igneous layering mechanisms. As a result of large variations in the modal composition of the igneous layers, combining AMS with anisotropy of anhysteretic remanence, CPOs and high spatial resolution stratigraphic logging is essential to gain a comprehensive perspective of the rock fabric. Our magnetic data show that arfvedsonite and magnetite both contribute to the AMS; their relative contributions vary through the layered stratigraphy. A comparison of the AMS fabric with the fabrics recorded in the field and the CPO shows that our magnetic fabric is inverse to the silicate fabric defined by arfvedsonite and alkali feldspar. Our data record a consistent sub-horizontal silicate mineral foliation and lineation. Crucially, the silicate fabric can be oblique to the modal layering in both strike and dip. The consistent presence of both a mineral foliation and a lineation through the modal layers, and the obliquity between the silicate fabric and the modal layering, calls into question previous studies that have cited *in situ* nucleation and growth as the main mechanism in igneous layering. Our data best support a closed magmatic system model in which igneous layers form through crystal mat accumulation. Obliquity between the silicate fabric and the modal layering suggests that the crystal pile was likely impacted by differential compaction due to roof rock collapse and subsequent intrusion-wide compaction.

Scientific editing by Kenta Yoshida

Acknowledgements The field context and samples for this study were collected during a field expedition to Ilímaussaq in 2022 and we thank Tesni Morgan, Aithne Lawrence, Nina Brendling, Yasamin Bayley and Brogan Smith for their support during this expedition. We also thank A. Borst and an anonymous reviewer for detailed and constructive reviews and K. Yoshida for editorial handling.

Author contributions EJ: conceptualization (lead), data curation (lead), formal analysis (lead), funding acquisition (lead), investigation (lead), methodology (lead), project administration (lead), visualization (lead), writing – original draft (lead); WM: conceptualization (supporting), formal analysis (supporting), methodology (supporting), resources (equal), supervision (lead), writing – review and editing (supporting); CM: formal analysis (supporting), methodology (supporting), supervision (supporting), visualization (supporting), writing – review and editing (supporting); TM: formal analysis (supporting), methodology (supporting), writing – review and editing (supporting); SP: formal analysis (supporting), methodology (supporting), resources (supporting), writing – review and editing (supporting); WH: supervision (supporting), writing – review and editing (supporting); MCH: formal analysis (supporting), supervision (supporting), writing – review and editing (supporting).

Funding The field expedition to Ilímaussaq, South Greenland in 2022 was funded by the Geological Society of London, the Gino Watkins Memorial Fund, the Arctic Club, the Society of Economic Geologists, the Cambridge Arctic Shelf Programme, the Henry Emeleus award of the Volcanic and Magmatic Studies Group, the Hazel-Prichard Student Bursary and the Edinburgh Geological Society. This work was supported by the Natural Environment Research Council via an IAPETUS2 PhD studentship held by Emily Jones (grant reference NE/S007431/1). William Hutchison is funded by a UKRI Future Leaders Fellowship (MR/S033505/1).

Competing interests The authors declare that they have no known competing financial interests or personal relationships that could have appeared to influence the work reported in this paper.

Data availability The datasets generated and/or analysed during the current study are available in the Mendeley Data repository, <https://doi.org/10.6084/m9.figshare.c.7618284>

References

- Ageeva, O., Habler, G., Pertsev, A. and Abart, R. 2017. Fe–Ti oxide micro-inclusions in clinopyroxene of oceanic gabbro: phase content, orientation relations and petrogenetic implication. *Lithos*, **290**–291, 104–115, <https://doi.org/10.1016/j.lithos.2017.08.007>
- Ageeva, O., Bian, G., Habler, G., Pertsev, A. and Abart, R. 2020. Crystallographic and shape orientations of magnetite micro-inclusions in plagioclase. *Contributions to Mineralogy and Petrology*, **175**, 95, <https://doi.org/10.1007/s00410-020-01735-8>
- Andersen, S., Bohse, H. and Steinfeld, A. 1981. A geological section through the southern part of the Ilmaussaq intrusion. *Rapport Grønlands Geologiske Undersøgelse*, **103**, 39–42, <https://doi.org/10.34194/rapggu.v103.7729>
- Andersen, S., Bohse, H. and Steinfeld, A. 1988. *The Southern Part of the Ilmaussaq Complex, South Greenland*, 1:20,000. Grønlands Geologiske Undersøgelse.
- Bachmann, O. and Huber, C. 2019. The inner workings of crustal distillation columns; the physical mechanisms and rates controlling phase separation in silicic magma reservoirs. *Journal of Petrology*, **60**, 3–18, <https://doi.org/10.1093/petrology/egy103>
- Bailey, J.C., Gwóźdz, R., Rose-Hansen, J. and Sørensen, H. 2001. Geochemical overview of the Ilmaussaq alkaline complex, South Greenland. *Geology of Greenland Survey Bulletin*, **190**, 35–53, <https://doi.org/10.34194/ggub.v190.5172>
- Benn, K., Ham, N.M., Pignotta, G.S. and Bleeker, W. 1998. Emplacement and deformation of granites during transpression: magnetic fabrics of the Archean Sparrow pluton, Slave Province, Canada. *Journal of Structural Geology*, **20**, 1247–1259, [https://doi.org/10.1016/S0191-8141\(98\)00665-0](https://doi.org/10.1016/S0191-8141(98)00665-0)
- Biedermann, A.R. 2018. Magnetic anisotropy in single crystals: a review. *Geosciences*, **8**, 1–16, <https://doi.org/10.3390/geosciences8080302>
- Biedermann, A.R., Koch, C.B., Pettke, T. and Hirt, A.M. 2015a. Magnetic anisotropy in natural amphibole crystals. *American Mineralogist*, **100**, 1940–1951, <https://doi.org/10.2138/am-2015-5173>
- Biedermann, A.R., Pettke, T., Bender Koch, C. and Hirt, A.M. 2015b. Magnetic anisotropy in clinopyroxene and orthopyroxene single crystals. *Journal of Geophysical Research: Solid Earth*, **120**, 1431–1451, <https://doi.org/10.1002/2014JB011678>
- Biedermann, A.R., Heidelbach, F., Jackson, M., Bilardello, D. and McEnroe, S.A. 2016. Magnetic fabrics in the Bjerkreim Sokndal layered intrusion, Rogaland, southern Norway: mineral sources and geological significance. *Tectonophysics*, **688**, 101–118, <https://doi.org/10.1016/j.tecto.2016.09.019>
- Biedermann, A.R., Kunze, K. and Hirt, A.M. 2018. Interpreting magnetic fabrics in amphibole-bearing rocks. *Tectonophysics*, **722**, 566–576, <https://doi.org/10.1016/j.tecto.2017.11.033>
- Bilardello, D. 2016. Magnetic anisotropy: theory, instrumentation, and techniques. In: Bilardello, D. (ed.) *Reference Module in Earth Systems and Environmental Sciences*. Elsevier, 1–14, <https://doi.org/10.1016/b978-0-12-409548-9.09516-6>
- Bohse, H., Brooks, C.K. and Kunzendorf, H. 1971. Field observations on the kakortokites of the Ilmaussaq intrusion, South Greenland, including mapping and analyses by portable X-ray fluorescence equipment for zirconium and niobium. *Rapport Grønlands Geologiske Undersøgelse*, **38**, 1–42.
- Bons, P.D., Baur, A. et al. 2015. Layered intrusions and traffic jams. *Geology*, **43**, 71–74, <https://doi.org/10.1130/G36276.1>
- Boorman, S., Boudreau, A. and Kruger, F.J. 2004. The Lower Zone–Critical Zone transition of the Bushveld Complex: a quantitative textural study. *Journal of Petrology*, **45**, 1209–1235, <https://doi.org/10.1093/petrology/egh011>
- Borradaile, G. 1987. Anisotropy of magnetic susceptibility: rock composition versus strain. *Tectonophysics*, **138**, 327–329, [https://doi.org/10.1016/0040-1951\(87\)90051-5](https://doi.org/10.1016/0040-1951(87)90051-5)
- Borradaile, G.J. 1988. Magnetic susceptibility, petrofabrics and strain. *Tectonophysics*, **156**, 1–20, [https://doi.org/10.1016/0040-1951\(88\)90279-X](https://doi.org/10.1016/0040-1951(88)90279-X)
- Borradaile, G.J. and Gauthier, D. 2001. AMS-detection of inverse fabrics without AARM, in ophiolite dikes. *Geophysical Research Letters*, **28**, 3517–3520, <https://doi.org/10.1029/2001GL012976>
- Borradaile, G.J. and Henry, B. 1997. Tectonic applications of magnetic susceptibility and its anisotropy. *Earth-Science Reviews*, **42**, 49–93, [https://doi.org/10.1016/S0012-8252\(96\)00044-X](https://doi.org/10.1016/S0012-8252(96)00044-X)
- Borradaile, G.J. and Jackson, M. 2004. Anisotropy of magnetic susceptibility (AMS): magnetic petrofabrics of deformed rocks. *Geological Society, London, Special Publications*, **238**, 299–360, <https://doi.org/10.1144/GSL.SP.2004.238.01.18>
- Borradaile, G., Keeler, W., Alford, C. and Sarvas, P. 1987. Anisotropy of magnetic susceptibility of some metamorphic minerals. *Physics of the Earth and Planetary Interiors*, **48**, 161–166, [https://doi.org/10.1016/0031-9201\(87\)90119-1](https://doi.org/10.1016/0031-9201(87)90119-1)
- Borst, A.M., Friis, H., Andersen, T., Nielsen, T.F.D., Waight, T.E. and Smit, M.A. 2016. Zirconosilicates in the kakortokites of the Ilmaussaq complex, South Greenland: implications for fluid evolution and high-field-strength and rare-earth element mineralization in agpaitic systems. *Mineralogical Magazine*, **80**, 5–30, <https://doi.org/10.1180/minmag.2016.080.046>
- Borst, A.M., Friis, H., Nielsen, T.F.D. and Waight, T.E. 2018. Bulk and mush melt evolution in agpaitic intrusions: insights from compositional zoning in eudialyte, Ilmaussaq complex, South Greenland. *Journal of Petrology*, **59**, 589–612, <https://doi.org/10.1093/petrology/egy038>
- Borst, A.M., Waight, T.E., Finch, A.A., Storey, M. and Roux, P.J.L. 2019. Dating agpaitic rocks: a multi-system (U/Pb, Sm/Nd, Rb/Sr and $^{40}\text{Ar}/^{39}\text{Ar}$) isotopic study of layered nepheline syenites from the Ilmaussaq complex, Greenland. *Lithos*, **324**–325, 74–88, <https://doi.org/10.1016/j.lithos.2018.10.037>
- Boudreau, A.E. 1988. Investigations of the Stillwater Complex. IV. The role of volatiles in the petrogenesis of the J-M Reef, Minneapolis adit section. *Canadian Mineralogist*, **26**, 193–208, <https://www.researchgate.net/publication/284801885>
- Boudreau, A.E. and McBirney, A.R. 1997. The Skaergaard Layered Series. Part III. Non-dynamic layering. *Journal of Petrology*, **38**, 1003–1020, <https://doi.org/10.1093/ptrotyj/38.8.1003>
- Branagan, D.F. 2005. History of geology from 1900 to 1962. In: Selley, R.C., Cocks, R.M. and Plimer, I.R. (eds) *Encyclopedia of Geology*. Elsevier, 185–196, <https://doi.org/10.1016/B0-12-369396-9/00370-1>
- Burton-Johnson, A., Macpherson, C.G., Muraszko, J.R., Harrison, R.J. and Jordan, T.A. 2019. Tectonic strain recorded by magnetic fabrics (AMS) in plutons, including Mt Kinabalu, Borneo: a tool to explore past tectonic regimes and syn-magmatic deformation. *Journal of Structural Geology*, **119**, 50–60, <https://doi.org/10.1016/j.jsg.2018.11.014>
- Černý, J., Melichar, R., Všianský, D. and Drahokoupil, J. 2020. Magnetic anisotropy of rocks: a new classification of inverse magnetic fabrics to help geological interpretations. *Journal of Geophysical Research: Solid Earth*, **125**, 1–13, <https://doi.org/10.1029/2020JB020426>
- Chadwick, B. and Garde, A.A. 1996. Palaeoproterozoic oblique plate convergence in South Greenland: a reappraisal of the Ketilidian Orogen. *Geological Society, London, Special Publications*, **112**, 179–196.
- Clark, D.A. 1997. Magnetic petrophysics and magnetic petrology: aids to geological interpretation of magnetic surveys. *Journal of Australian Geology & Geophysics*, **17**, 83–103.
- Duchesne, J.C. and Charlier, B. 2005. Geochemistry of cumulates from the Bjerkreim–Sokndal layered intrusion (S. Norway). Part I: constraints from major elements on the mechanism of cumulate formation and on the jotunite liquid line of descent. *Lithos*, **83**, 229–254, <https://doi.org/10.1016/j.lithos.2005.03.004>
- Dunlop, D.J. and Özdemir, Ö. 1997. *Rock Magnetism*. Cambridge University Press.
- Eales, H.V. and Cawthorn, R.G. 1996. The Bushveld Complex. In: Cawthorn, R.G. (ed.) *Layered Intrusions*. Elsevier, 181–229.
- Ferré, E.C. 2002. Theoretical models of intermediate and inverse AMS fabrics. *Geophysical Research Letters*, **29**, 1–4, <https://doi.org/10.1029/2001GL014367>
- Ferré, E.C., Maes, S.M. and Butak, K.C. 2009. The magnetic stratification of layered mafic intrusions: natural examples and numerical models. *Lithos*, **111**, 83–94, <https://doi.org/10.1016/j.lithos.2009.03.042>
- Ferré, E.C., Michelsen, K.J., Ernst, W.G., Boyd, J.D. and Canon-Tapia, E. 2012. Vertical zonation of the Barcroft granodiorite, White Mountains, California: implications for magmatic processes. *American Mineralogist*, **97**, 1049–1059, <https://doi.org/10.2138/am.2012.4013>
- Garde, A.A., Hamilton, M.A., Chadwick, B., Grocott, J. and McCaffrey, K.J.W. 2002. The Ketilidian orogen of South Greenland: geochronology, tectonics, magmatism, and fore-arc accretion during Palaeoproterozoic oblique convergence. *Canadian Journal of Earth Sciences*, **39**, 765–793, <https://doi.org/10.1139/e02-026>
- Gordon, S.G. 1927. On arfvedsonite, riebeckite, and crocidolite from Greenland. *Proceedings of the Academy of Natural Sciences of Philadelphia*, **79**, 193–205.
- Hess, H.H. 1960. Stillwater Igneous Complex, Montana. *GSA, Memoirs*, **80**, <https://doi.org/10.1130/MEM80>
- Higgins, M.D. 1991. The origin of laminated and massive anorthosite, Sept Iles layered intrusion, Quebec, Canada. *Contributions to Mineralogy and Petrology*, **106**, 340–354.
- Higgins, M.D. 2011. Textural coarsening in igneous rocks. *International Geology Review*, **53**, 354–376, <https://doi.org/10.1080/00206814.2010.496177>
- Hogarth, D.D., Chao, G.Y. and Townsend, M.G. 1987. Potassium- and fluorine-rich amphiboles from the Gatineau area, Quebec. *Canadian Mineralogist*, **25**, 739–753.
- Holness, M.B. 2014. The effect of crystallization time on plagioclase grain shape in dolerites. *Contributions to Mineralogy and Petrology*, **168**, 1–19, <https://doi.org/10.1007/s00410-014-1076-5>
- Holness, M.B. 2018. Melt segregation from silicic crystal mushes: a critical appraisal of possible mechanisms and their microstructural record. *Contributions to Mineralogy and Petrology*, **173**, <https://doi.org/10.1007/s00410-018-1465-2>
- Holness, M.B., Sides, R., Prior, D.J., Cheadle, M.J. and Upton, B.G.J. 2012. The peridotite plugs of Rum: crystal settling and fabric development in magma conduits. *Lithos*, **134**–135, 23–40, <https://doi.org/10.1016/j.lithos.2011.11.024>

- Holness, M.B., Vukmanovic, Z. and Mariani, E. 2017. Assessing the role of compaction in the formation of adcumulates: a microstructural perspective. *Journal of Petrology*, **58**, 643–674, <https://doi.org/10.1093/petrology/egx037>
- Holness, M.B., Vukmanovic, Z. and O'Driscoll, B. 2023. The formation of chromite chains and clusters in igneous rocks. *Journal of Petrology*, **64**, egac124, <https://doi.org/10.1093/petrology/egac124>
- Hunt, E.J., Finch, A.A. and Donaldson, C.H. 2017. Layering in peralkaline magmas, Ilmaussaq complex, S Greenland. *Lithos*, **268–271**, 1–15, <https://doi.org/10.1016/j.lithos.2016.10.023>
- Irvine, T.N. 1980. Magmatic infiltration metasomatism, double-diffusive fractional crystallization, and adcumulus growth in the Muskox intrusion and other layered intrusions. In: Hargraves, R.B. (ed.) *Physics of Magmatic Processes*. Princeton University Press, 325–383, <https://doi.org/10.1515/9781400854493.325>
- Jackson, E. 1961. Primary textures and mineral associations in the ultramafic zone of the Stillwater Complex. *United States Geological Survey, Professional Papers*, **358**, <https://doi.org/10.3133/pp358>
- Jackson, M. 1991. Anisotropy of magnetic remanence: a brief review of mineralogical sources, physical origins, and geological applications, and comparison with susceptibility anisotropy. *Pure and Applied Geophysics*, **36**, 1–28, <https://doi.org/10.1007/BF00878885>
- Jelinek, V. 1977. *The Statistical Theory of Measuring Anisotropy of Magnetic Susceptibility of Rocks and Its Application*. Geofyzika, Brno.
- Jelinek, V. 1981. Characterization of the magnetic fabric of rocks. *Tectonophysics*, **79**, 63–67.
- Knight, M.D. and Walker, G.P.L. 1988. Magma flow directions in dikes of the Koolau complex, Oahu, determined from magnetic fabric studies. *Journal of Geophysical Research*, **93**, 4301–4319, <https://doi.org/10.1029/JB093iB05p04301>
- Koopmans, L., McCarthy, W. and Magee, C. 2022. Dyke architecture, mineral layering, and magmatic convection; new perspectives from the Younger Giant Dyke Complex, S Greenland. *Geochemistry, Geophysics, Geosystems*, **23**, e2021GC010260, <https://doi.org/10.1029/2021GC010260>
- Kruger, W. and Latypov, R. 2022. In situ crystallization of non-cotectic and foliated igneous rocks on a magma chamber floor. *Communications Earth and Environment*, **3**, 1–12, <https://doi.org/10.1038/s43247-022-00584-6>
- Krumrei, T.V., Villa, I.M., Marks, M.A.W. and Markl, G. 2006. A $^{40}\text{Ar}/^{39}\text{Ar}$ and U/Pb isotopic study of the Ilmaussaq complex, South Greenland: implications for the ^{40}K decay constant and for the duration of magmatic activity in a peralkaline complex. *Chemical Geology*, **227**, 258–273, <https://doi.org/10.1016/j.chemgeo.2005.10.004>
- Larsen, L.M. and Sørensen, H. 1987. The Ilmaussaq intrusion – progressive crystallization and formation of layering in an apaitic magma. *Geological Society, London, Special Publications*, **30**, 473–488, <http://sp.lyellcollection.org/>
- Latimer, B., McCarthy, W., Mattsson, T. and Reavy, J. 2024. Enclaves as mushy magma strain archives: new perspectives on composite magmatic fabrics in plutons. *Geosphere*, **20**, 1390–1410, <https://doi.org/10.1130/GES02786.1>
- Latypov, R., Chistyakova, S., Barnes, S.J. and Hunt, E.J. 2017. Origin of platinum deposits in layered intrusions by in situ crystallization: evidence from undercutting Merensky Reef of the Bushveld Complex. *Journal of Petrology*, **58**, 715–762, <https://doi.org/10.1093/petrology/egx032>
- Lindhuber, M.J., Marks, M.A.W., Bons, P.D., Wenzel, T. and Markl, G. 2015. Crystal mat-formation as an igneous layering-forming process: textural and geochemical evidence from the “lower layered” nepheline syenite sequence of the Ilmaussaq complex, South Greenland. *Lithos*, **224–225**, 295–309, <https://doi.org/10.1016/j.lithos.2015.03.007>
- Lofgren, G.E. and Donaldson, C.H. 1975. Curved branching crystals and differentiation in comb-layered rocks. *Contributions to Mineralogy and Petrology*, **49**, 309–319, <https://doi.org/10.1007/BF00376183>
- Maes, S.M., Ferré, E.C., Tikoff, B., Brown, P.E. and Marsh, J.S. 2008. Rock magnetic stratigraphy of a mafic layered sill: a key to the Karoo volcanics plumbing system. *Journal of Volcanology and Geothermal Research*, **172**, 75–92, <https://doi.org/10.1016/j.jvolgeores.2005.07.038>
- Magee, C., O'Driscoll, B., Petronis, M.S. and Stevenson, C.T.E. 2016. Three-dimensional magma flow dynamics within subvolcanic sheet intrusions. *Geosphere*, **12**, 842–866, <https://doi.org/10.1130/GES01270.1>
- Mangler, M.F., Humphreys, M.C.S., Wadsworth, F.B., Iveson, A.A. and Higgins, M.D. 2022. Variation of plagioclase shape with size in intermediate magmas: a window into incipient plagioclase crystallisation. *Contributions to Mineralogy and Petrology*, **177**, 64, <https://doi.org/10.1007/s00410-022-01922-9>
- Marks, M.A.W. and Markl, G. 2015. The Ilmaussaq alkaline complex, South Greenland. In: Charlier, B., Namur, O., Latypov, R. and Tegner, C. (eds) *Layered Intrusions*. Springer, 649–691, https://doi.org/10.1007/978-94-017-9652-1_14
- Marks, M.A.W., Hettmann, K., Schilling, J., Frost, B.R. and Markl, G. 2011. The mineralogical diversity of alkaline igneous rocks: critical factors for the transition from miaskitic to apaitic phase assemblages. *Journal of Petrology*, **52**, 439–455, <https://doi.org/10.1093/petrology/egq086>
- Martín-Hernández, F., Lüneburg, C.M., Aubourg, C. and Jackson, M. 2004. Magnetic fabric: methods and applications – an introduction. *Geological Society, London, Special Publications*, **238**, 1–7, <https://doi.org/10.1144/GSL.SP.2004.238.01.01>
- Mattsson, T., Petri, B. *et al.* 2021. Decrypting magnetic fabrics (AMS, AARM, AIRM) through the analysis of mineral shape fabrics and distribution anisotropy. *Journal of Geophysical Research: Solid Earth*, **126**, e2021JB021895, <https://doi.org/10.1029/2021JB021895>
- McCarthy, W., Reavy, R.J., Stevenson, C.T. and Petronis, M.S. 2015. Late Caledonian transpression and the structural controls on pluton construction; new insights from the Omey Pluton, western Ireland. *Earth and Environmental Science Transactions of the Royal Society of Edinburgh*, **106**, 11–28, <https://doi.org/10.1017/S1755691015000201>
- Meurer, W.P. and Boudreau, A.E. 1998. Compaction of igneous cumulates part II: compaction and the development of igneous foliations. *The Journal of Geology*, **106**, 293–304, <https://doi.org/10.1086/516023>
- Namur, O. *et al.* 2015. Igneous layering in basaltic magma chambers. In: Charlier, B., Namur, O., Latypov, R. and Tegner, C. (eds) *Layered Intrusions*. Springer, 75–152, https://doi.org/10.1007/978-94-017-9652-1_2
- Naslund, H.R. and McBirney, A.R. 1996. Mechanisms of formation of igneous layering. In: Cawthorn, R.G. (ed.) *Layered Intrusions*. Elsevier, 1–43.
- Nielsen, T.F.D., Andersen, J.C.Ø. *et al.* 2015. The Skaergaard PGE and gold deposit: the result of in situ fractionation, sulphide saturation, and magma chamber-scale precious metal redistribution by immiscible Fe-rich melt. *Journal of Petrology*, **56**, 1643–1676, <https://doi.org/10.1093/petrology/egv049>
- O'Driscoll, B. and Van Tongeren, J.A. 2017. Layered intrusions: from petrological paradigms to precious metal repositories. *Elements*, **13**, 383–389, <https://doi.org/10.2138/gselements.13.6.383>
- O'Driscoll, B., Donaldson, C.H., Troll, V.R., Jerram, D.A. and Emeleus, C.H. 2007. An origin for harrisitic and granular olivine in the Rum layered suite, NW Scotland: a crystal size distribution study. *Journal of Petrology*, **48**, 253–270, <https://doi.org/10.1093/petrology/egl059>
- O'Driscoll, B., Stevenson, C.T.E. and Troll, V.R. 2008. Mineral lamination development in layered gabbros of the British Palaeogene Igneous Province: a combined anisotropy of magnetic susceptibility, quantitative textural and mineral chemistry study. *Journal of Petrology*, **49**, 1187–1221, <https://doi.org/10.1093/petrology/egn022>
- O'Driscoll, B., Ferré, E.C., Stevenson, C.T.E. and Magee, C. 2015. The significance of magnetic fabric in layered mafic-ultramafic intrusions. In: Charlier, B., Namur, O., Latypov, R. and Tegner, C. (eds) *Layered Intrusions*. Springer, 295–329, https://doi.org/10.1007/978-94-017-9652-1_7
- O'Driscoll, B., Petronis, M.S. *et al.* 2024. Magnetic fabrics in laminated rocks of the Ilmaussaq Igneous Complex, Southern Greenland. *The Canadian Journal of Mineralogy and Petrology*, **62**, 821–846, <https://doi.org/10.3749/2400008>
- Pang, K.N., Li, C., Zhou, M.F. and Ripley, E.M. 2009. Mineral compositional constraints on petrogenesis and oxide ore genesis of the late Permian Panzhihua layered gabbroic intrusion, SW China. *Lithos*, **110**, 199–214, <https://doi.org/10.1016/j.lithos.2009.01.007>
- Parés, J.M. 2015. Sixty years of anisotropy of magnetic susceptibility in deformed sedimentary rocks. *Frontiers in Earth Science*, **3**, <https://doi.org/10.3389/feart.2015.00004>
- Petronis, M.S., O'Driscoll, B., Stevenson, C.T.E. and Reavy, R.J. 2012. Controls on emplacement of the Caledonian Ross of Mull Granite, NW Scotland: anisotropy of magnetic susceptibility and magmatic and regional structures. *GSA Bulletin*, **124**, 906–927, <https://doi.org/10.1130/B30362.1>
- Pfaff, K., Krumrei, T., Marks, M., Wenzel, T., Rudolf, T. and Markl, G. 2008. Chemical and physical evolution of the “lower layered sequence” from the nepheline syenitic Ilmaussaq intrusion, South Greenland: implications for the origin of magmatic layering in peralkaline felsic liquids. *Lithos*, **106**, 280–296, <https://doi.org/10.1016/j.lithos.2008.07.018>
- Ratschbacher, B.C., Marks, M.A.W., Bons, P.D., Wenzel, T. and Markl, G. 2015. Emplacement and geochemical evolution of highly evolved syenites investigated by a combined structural and geochemical field study: the lujavrites of the Ilmaussaq Complex, SW Greenland. *Lithos*, **231**, 62–76, <https://doi.org/10.1016/j.lithos.2015.06.004>
- Rosenblum, S. and Brownfield, I.K. 2000. *Magnetic Susceptibility of Minerals*. US Geological Survey.
- Schonwandt, H.K., Barnes, G.B. and Ulrich, T. 2016. A description of the world-class rare earth element deposit, Tanbreez, South Greenland. In: Borges De Lima, I. and Leal Filho, W. (eds) *Rare Earths Industry: Technological, Economic, and Environmental Implications*. Elsevier, 73–85, <https://doi.org/10.1016/B978-0-12-802328-0.00005-X>
- Selkin, P.A., Gee, J.S. and Meurer, W.P. 2014. Magnetic anisotropy as a tracer of crystal accumulation and transport, Middle Banded Series, Stillwater Complex, Montana. *Tectonophysics*, **629**, 123–137, <https://doi.org/10.1016/j.tecto.2014.03.028>
- Smith, W.D. and Maier, W.D. 2021. The geotectonic setting, age and mineral deposit inventory of global layered intrusions. *Earth-Science Reviews*, **220**, 1–36, <https://doi.org/10.1016/j.earscirev.2021.103736>
- Sørensen, H. 2001. Brief introduction to the geology of the Ilmaussaq alkaline complex, South Greenland, and its exploration history. *Geology of Greenland Survey Bulletin*, **190**, 7–23, <https://doi.org/10.34194/ggub.v190.5170>
- Sørensen, H., Bohse, H. and Bailey, J.C. 2006. The origin and mode of emplacement of lujavrites in the Ilmaussaq alkaline complex, South Greenland. *Lithos*, **91**, 286–300, <https://doi.org/10.1016/j.lithos.2006.03.021>
- Sørensen, H., Bailey, J.C. and Rose-Hansen, J. 2011. The emplacement and crystallization of the U–Th–REE-rich apaitic and hyperapaitic lujavrites at Kvanefjeld, Ilmaussaq alkaline complex, South Greenland. *Bulletin of the Geological Society of Denmark*, **59**, 69–92, <https://doi.org/10.37570/bgscd-2011-59-08>
- Tait, S. and Jaupart, C. 1992. Compositional convection in a reactive crystalline mush and melt differentiation. *Journal of Geophysical Research*, **97**, 6735–6756, <https://doi.org/10.1029/92JB00016>

- Tarling, D.H. and Hrouda, F. 1993. *The Magnetic Anisotropy of Rocks*. Chapman & Hall.
- Upton, B.G.J. 2013. Tectono-magmatic evolution of the younger Gardar southern rift, South Greenland. *GEUS Bulletin*, **29**, 1–124, <https://doi.org/10.34194/geusb.v29.4692>
- Upton, B.G.J., Emeleus, C.H., Heaman, L.M., Goodenough, K.M. and Finch, A.A. 2003. Magmatism of the mid-Proterozoic Gardar Province, South Greenland: chronology, petrogenesis and geological setting. *Lithos*, **68**, 43–65, [https://doi.org/10.1016/S0024-4937\(03\)00030-6](https://doi.org/10.1016/S0024-4937(03)00030-6)
- Vukmanovic, Z., Holness, M.B., Stock, M.J. and Roberts, R.J. 2019. The creation and evolution of crystal mush in the Upper Zone of the Rustenburg layered suite, Bushveld Complex, South Africa. *Journal of Petrology*, **60**, 1523–1542, <https://doi.org/10.1093/petrology/egz038>
- Wager, L.R., Brown, G.M. and Wadsworth, W.J. 1960. Types of igneous cumulates. *Journal of Petrology*, **1**, 73–85, <http://petrology.oxfordjournals.org/>
- Wieser, P.E., Vukmanovic, Z., Kilian, R., Ringe, E., Holness, M.B., MacLennan, J. and Edmonds, M. 2019. To sink, swim, twin, or nucleate: a critical appraisal of crystal aggregation processes. *Geology*, **47**, 948–952, <https://doi.org/10.1130/G46660.1>
- Young, I.M. and Donaldson, C.H. 1985. Formation of granular-textured layers and laminae within the Rhum crystal pile. *Geological Magazine*, **122**, 519–528, <https://doi.org/10.1017/S0016756800035433>
- Žák, J., Schulmann, K. and Hrouda, F. 2005. Multiple magmatic fabrics in the Sázava pluton (Bohemian Massif, Czech Republic): a result of superposition of wrench-dominated regional transpression on final emplacement. *Journal of Structural Geology*, **27**, 805–822, <https://doi.org/10.1016/j.jsg.2005.01.012>
- Zhang, B., Hu, X., Asimow, P.D., Zhang, X., Xu, J., Zhou, W. and Fan, D. 2019. Crystal size distribution of amphibole grown from hydrous basaltic melt at 0.6–2.6 GPa and 860–970°C. *American Mineralogist*, **104**, 525–535, <https://doi.org/10.2138/am-2019-6759>